J. Fluid Mech. (2010), *vol.* 650, *pp.* 215–250. © Cambridge University Press 2010
doi:10.1017/S0022112009993521

Energy dissipation in microfluidic beam resonators

JOHN E. SADER[1]†, THOMAS P. BURG[2,3] AND SCOTT R. MANALIS[2,4]

[1]Department of Mathematics and Statistics, The University of Melbourne, Victoria 3010, Australia

[2]Department of Biological Engineering, Massachusetts Institute of Technology, Cambridge, MA 02139, USA

[3]Max Planck Institute for Biophysical Chemistry, 37077 Goettingen, Germany

[4]Department of Mechanical Engineering, Massachusetts Institute of Technology, Cambridge, MA 02139, USA

(Received 18 May 2009; revised 16 November 2009; accepted 17 November 2009; first published online 22 March 2010)

The fluid–structure interaction of resonating microcantilevers immersed in fluid has been widely studied and is a cornerstone in nanomechanical sensor development. In many applications, fluid damping imposes severe limitations by strongly degrading the signal-to-noise ratio of measurements. Recently, Burg *et al.* (*Nature*, vol. 446, 2007, pp. 1066–1069) proposed an alternative type of microcantilever device whereby a microfluidic channel was embedded inside the cantilever with vacuum outside. Remarkably, it was observed that energy dissipation in these systems was almost identical when air or liquid was passed through the channel and was 4 orders of magnitude lower than that in conventional microcantilever systems. Here, we study the fluid dynamics of these devices and present a rigorous theoretical model corroborated by experimental measurements to explain these observations. In so doing, we elucidate the dominant physical mechanisms giving rise to the unique features of these devices. Significantly, it is found that energy dissipation is not a monotonic function of fluid viscosity, but exhibits oscillatory behaviour, as fluid viscosity is increased/decreased. In the regime of low viscosity, inertia dominates the fluid motion inside the cantilever, resulting in thin viscous boundary layers – this leads to an increase in energy dissipation with increasing viscosity. In the high-viscosity regime, the boundary layers on all surfaces merge, leading to a decrease in dissipation with increasing viscosity. Effects of fluid compressibility also become significant in this latter regime and lead to rich flow behaviour. A direct consequence of these findings is that miniaturization does not necessarily result in degradation in the quality factor, which may indeed be enhanced. This highly desirable feature is unprecedented in current nanomechanical devices and permits direct miniaturization to enhance sensitivity to environmental changes, such as mass variations, in liquid.

1. Introduction

The dynamic properties of micromechanical structures immersed in fluid underpin a broad range of applications ranging from sensing of environmental conditions

† Email address for correspondence: jsader@unimelb.edu.au

https://doi.org/10.1017/S0022112009993521 Published online by Cambridge University Press

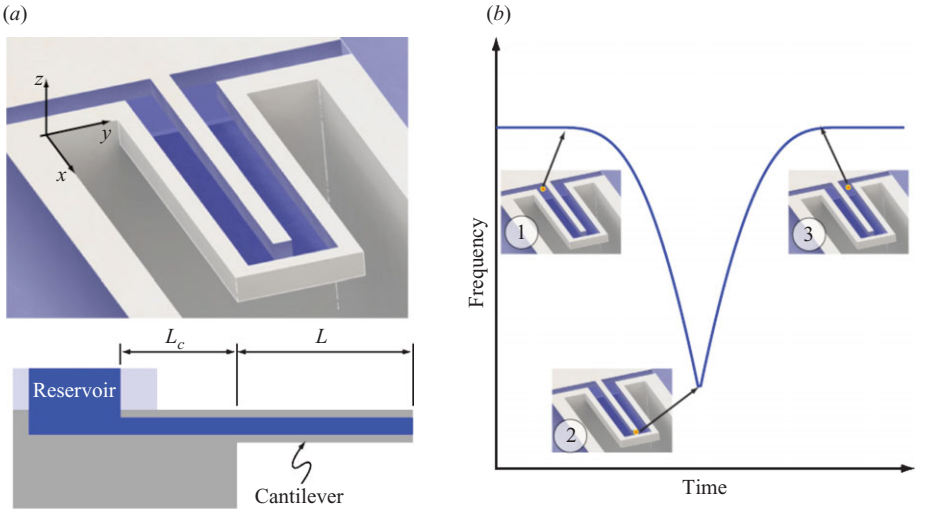


FIGURE 1. Illustration of fluid channel embedded microcantilever. (*a*) Perspective (top): layout of the embedded fluid channel, which is normally closed and shown open here for illustration. Side view (bottom): cantilever structure (grey) showing cantilever length L and length of rigid lead channel L_c. Fluid channel is completely filled with fluid (blue). Cantilever end is simplified for modelling purposes: the cantilever tip is closed. (*b*) Application to measure the mass of a single cell. Position of the cell (red) as it flows through the fluid channel (blue) defines a transient resonant frequency change, the magnitude of which is proportional to the buoyant mass of the cell. Position 1, cell enters the suspended part of the channel; position 2, cell reaches the apex of the cantilever; position 3, cell exits the suspended channel.

with extreme precision (Berger *et al.* 1997; Lavrik, Sepaniak & Datkos 2004) to imaging with molecular and atomic resolution (Binnig, Quate & Gerber 1986; Fukuma *et al.* 2005). Importantly, the intrinsic flow properties of such small devices differ considerably from those of their macroscale counterparts, which in turn strongly affects their dynamics. One field where this is broadly evident is in the fluid dynamics of oscillating microcantilevers, which is strongly influenced by the effects of viscosity; this contrasts to macroscale cantilevers whose dynamics are very weakly affected by fluid viscosity (e.g. Chu 1963; Lindholm *et al.* 1965; Landweber 1967; Crighton 1983; Fu & Price 1987; Sader 1998; Chon, Mulvaney & Sader 2000; Naik, Longmire & Mantell 2003; Paul & Cross 2004; Clarke *et al.* 2005; Green & Sader 2005; Basak, Raman & Garimella 2006). Quality factors of microcantilevers thus are orders of magnitude smaller than those of macroscale cantilevers (Butt *et al.* 1993), and energy dissipation is strongly and monotonically enhanced with miniaturization (Sader 1998). Because the quality factor ultimately determines the precision to which small changes in resonant frequency can be measured, this presents significant challenges in using microcantilevers as sensors in liquid environments, where the quality factor often is of order unity (Butt *et al.* 1993).

Recently, it has been demonstrated that microcantilevers which incorporate a microfluidic channel in their interior can address this shortcoming. When filled with water and surrounded by vacuum, such devices have been shown to exhibit quality factors as high as 10 000 (Burg *et al.* 2007); see figure 1(*a*). Such quality factors are comparable to those of macroscale cantilevers (metres in length) and orders of magnitude higher than conventional microcantilevers (sub-millimetre lengths) in fluid. This ensures a very pure resonance that greatly enhances the signal-to-noise ratio of resonant frequency measurements.

https://doi.org/10.1017/S0022112009993521 Published online by Cambridge University Press

These vacuum-packaged microfluidic cantilever devices have enabled precise weighing of surface-adsorbed layers of biomolecules (Burg & Manalis 2003), cells and particles suspended in fluid (Burg *et al.* 2007). Specifically, measurements of particle mass are conducted by flowing a dilute suspension of particles through the resonator while measuring the shift in resonant frequency. When particles reach the tip, the frequency shift is at a maximum, and the magnitude of this shift informs about the buoyant mass of the particle; see figure 1(*b*). Particles can be prevented from sticking by appropriate surface treatment. On the other hand, molecular adsorption is detected by continuously flowing a solution through the channel and using the resonant frequency to monitor mass build-up due to surface adsorption. Other applications of fluid-filled microresonators include measurement of fluid density and mass flow on the microscopic (Enoksson, Stemme & Stemme 1996; Westberg *et al.* 1997; Sparks *et al.* 2003) and macroscopic scale (e.g. Mettler-Toledo DE51, Switzerland, http://www.mt.com). Efforts are currently being directed towards measuring subtle changes in single cell growth properties and to the miniaturization of the microchannel to enable the weighing of single viruses and ultimately single molecules.

Significantly, it was observed that the quality factor, and hence energy dissipation, in these devices was unchanged when air or water was passed through the embedded fluid channel. Such behaviour is unprecedented and is in stark contrast to conventional microcantilevers whose quality factor drops by 2 orders of magnitude when the surrounding fluid is changed from air to water (Butt *et al.* 1993). Here, we theoretically study motion of the fluid contained inside these new devices and explore the rich behaviour that emerges from such structures. In so doing, we discover that the complexity in flow dynamics of such devices greatly exceeds that of oscillating microcantilevers immersed in fluid.

The theoretical model is derived within the framework of Euler–Bernoulli beam theory (Timoshenko & Young 1968) that implicitly assumes a beam of infinite length relative to its width/thickness. The effects of shear deformation in the beam are thus neglected. A commensurate treatment of the fluid flow in this asymptotic limit is also given, ensuring a self-consistent treatment of the fluid–structure interaction. The effects of both fluid density and viscosity are considered, in line with previous treatments of the vibration of microcantilevers immersed in fluid (e.g. Sader 1998; Paul & Cross 2004). In contrast, however, the effects of fluid compressibility are also included and found to be of paramount importance in certain practical cases. This milieu of competing effects results in extremely rich flow behaviour that is not seen in the complementary problem of a microcantilever immersed in fluid. The result is that energy dissipation is not a monotonically increasing function of the fluid viscosity, as may be expected intuitively. This has significant implications to miniaturization, allowing for a reduction in energy dissipation which is unparalleled in micromechanical systems.

Importantly, the model focuses on energy dissipation due to the fluid motion only, and neglects the effects of structural dissipation in the solid cantilever structure. This latter dissipative mechanism can comprise numerous effects, such as thermoelastic dissipation, clamping losses, internal friction, and damping due to residual gas present in the vacuum cavity surrounding the cantilever (Yasumura *et al.* 2000). The combined contributions from these various effects are still poorly understood, but are expected to be approximately constant if the resonant frequency is varied only slightly (the practical case). The coupling of the fluid to these effects has not been explored in the literature, and is thus ignored in this study.

Using this theoretical model, we explain the prominent features of experimental measurements reported in a companion study (Burg, Sader & Manalis 2009), provide

https://doi.org/10.1017/S0022112009993521 Published online by Cambridge University Press

a quantitative comparison and theoretically explore the various flow regimes and flow properties in detail. Good agreement is found between this leading order theory and measurement, and the practical implications of the theoretical findings are discussed. Most strikingly, non-monotonicity of the quality factor with increasing fluid viscosity is accurately captured. In so doing, the new theoretical model elucidates the dominant underlying fluid physics giving rise to this unique behaviour. It is found that positioning of the fluid channel in the beam cross-section strongly affects the flow dynamics and hence the energy dissipation. This can lead to significant modification of the flow field in the embedded channel through the effects of fluid compressibility and significant enhancement of the pressure. Interestingly, it is found that through appropriate adjustment of the beam/channel dimensions and operating conditions, fluid pressures in the vicinity of 1 atm are possible, as we shall discuss. This has obvious implications to the generation of cavitation bubbles, which may find use in practical application.

We begin by summarizing the principal assumptions used in the theoretical model. This is followed by decomposition of the flow problem into an on-axis and off-axis problem, corresponding to placement of the fluid channel on and away from the beam neutral axis, respectively. The two sub-problems are then solved separately and later combined to obtain the complete flow field. We focus our discussion on the energy dissipation, while explaining the underlying physical mechanisms giving rise to its most important features. After this discussion, we provide a detailed comparison with available experimental measurements and close with a brief synopsis of theoretical considerations for further work.

2. Theory

The quality factor is defined as

$$Q = 2\pi \left. \frac{E_{stored}}{E_{diss/cycle}} \right|_{\omega=\omega_R}, \tag{1}$$

where E_{stored} is the maximum energy stored in the beam, $E_{diss/cycle}$ is the energy dissipated per cycle and ω_R is the radial resonant frequency. Throughout, we focus on the quality factor due to dissipation in the fluid channel only.

Consider a rectangular cantilever with a thin embedded channel that contains fluid; see figure 2. The model is derived under the following geometric assumptions:

(*a*) Cantilever length L is much larger than its width b_{cant} and thickness h_{cant}.

(*b*) Fluid channel thickness h_{fluid} is much smaller than the channel width b_{fluid} – as a leading order approximation, we take the formal limit $h_{fluid}/b_{fluid} \to 0$ throughout.

(*c*) Fluid channel spans the entire length of the cantilever L and the cantilever is vibrating in its fundamental mode.

(*d*) The lead channel of length L_c within the substrate of the chip is rigid.

(*e*) The amplitude of oscillation is much smaller than any geometric length scale of the beam, so that the convective inertial term in the Navier–Stokes equation can be ignored and linear motion and flow is ensured (Sader 1998).

Assumption (*b*) enables the embedded fluid channel to be represented by a single channel whose total width is the sum of the two parallel channels widths; cf. figures 1 and 2. As a direct consequence of assumption (*a*), the deformation of the beam material can be described formally using Euler–Bernoulli beam theory (Timoshenko & Young 1968). The displacement field is then given by

$$\boldsymbol{u}(x, z, t) = W(x, t)\hat{\boldsymbol{z}} - z\frac{\partial W}{\partial x}\hat{\boldsymbol{x}}, \tag{2}$$

https://doi.org/10.1017/S0022112009993521 Published online by Cambridge University Press

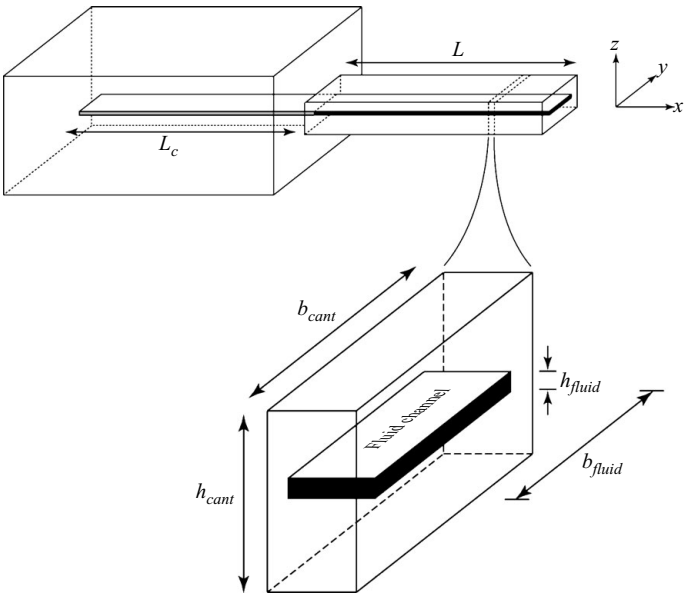


FIGURE 2. Schematic illustration of rectangular cantilever ($x > 0$) with embedded fluid channel and rigid lead channel ($x < 0$) showing dimensions. Origin of Cartesian coordinate system is centre-of-mass of clamped end.

where $W(x, t)$ is the deflection function of the beam; W is zero inside the rigid lead channel.

Because we are examining oscillatory motion, all dependent variables (denoted by X) are then expressed in terms of the explicit time dependence $\mathrm{e}^{-\mathrm{i}\omega t}$, such that

$$X(x, z, t) = \tilde{X}(x, z|\omega)\mathrm{e}^{-\mathrm{i}\omega t},$$

where ω is the radial frequency, t is time and i is the usual imaginary unit. For simplicity we shall henceforth omit the superfluous '$\sim$' notation, noting that the above relation holds universally. Consequently, the velocity field of the beam in (2) becomes

$$\boldsymbol{v}(x, z|\omega) = -\mathrm{i}\omega\left(W(x|\omega)\hat{\boldsymbol{z}} - z\frac{\partial W}{\partial x}\hat{\boldsymbol{x}}\right). \tag{3}$$

The fluid flow problem in the channel is to be solved subject to the solid boundary conditions specified in (3) by invoking the usual no-slip condition: the deflection function of the beam is independent of the fluid – the elastic modulus of common liquids is 2 orders of magnitude smaller than that of the solid cantilever walls and the stress generated in the fluid is much smaller than that in the solid.

Because the flow problem is linear it can be separated into two sub-problems, as illustrated in figure 3. The 'on-axis' sub-problem is identical to the flow when the channel midplane lies on the neutral axis of the beam ($z_0 = 0$), and the 'off-axis correction' sub-problem gives the additional flow due to off-axis placement of the channel ($z_0 \neq 0$). We will solve these problems separately and later combine them to obtain the complete flow that includes the effects of off-axis channel placement.

https://doi.org/10.1017/S0022112009993521 Published online by Cambridge University Press

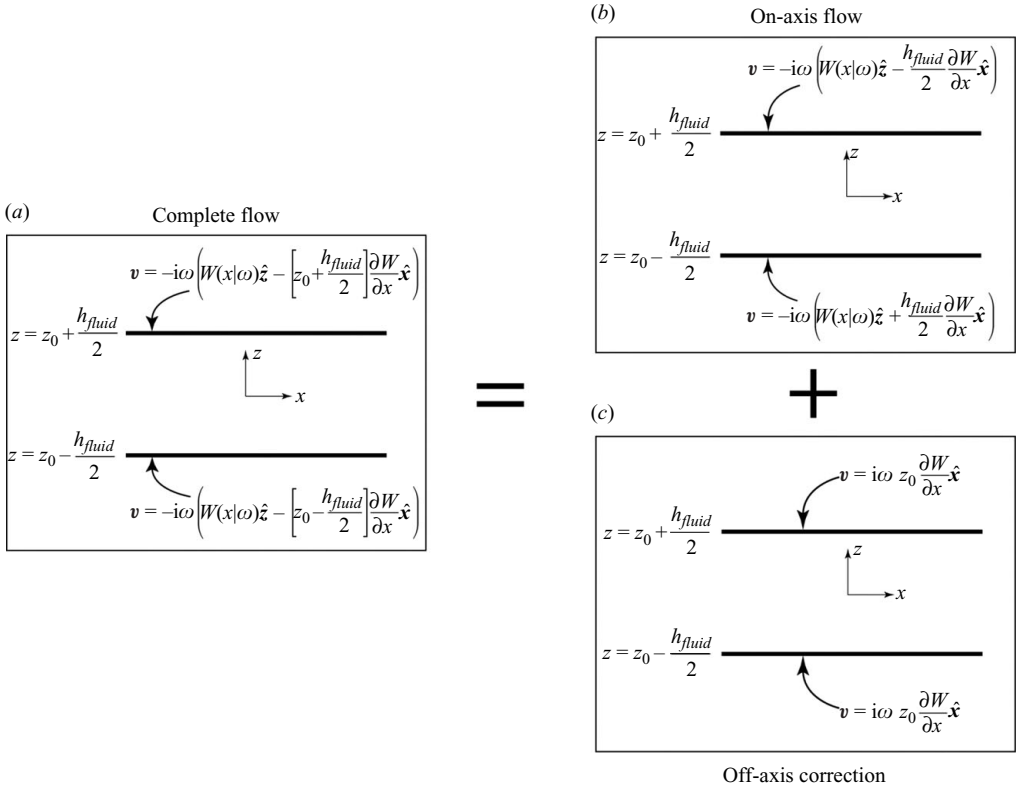


FIGURE 3. Schematic showing (*a*) the complete flow problem and its decomposition into (*b*) the on-axis flow problem, plus (*c*) the off-axis correction. The figures show a segment of the side view of the channel and give the flow boundary conditions and dimensions.

2.1. *On-axis placement of channel*

Because the flow field for the on-axis sub-problem is independent of z_0, we set $z_0 = 0$ for simplicity. This corresponds to the case where the channel midplane lies on the neutral axis of the beam, the flow problem for which is illustrated in figure 3(*b*).

We scale all dimensions of the flow field by the fluid channel thickness h_{fluid}, and denote all scaled variables with an overscore. For simplicity, we make the following definitions:

$$U(\bar{x}|\omega) = -\mathrm{i}\omega W(\bar{x}|\omega), \tag{4a}$$

$$\beta = \frac{\rho\omega h_{fluid}^2}{\mu}, \tag{4b}$$

where the latter parameter is the Reynolds number (Batchelor 1974) and indicates the importance of fluid inertia; geometrically, it corresponds to the squared ratio of channel thickness to the viscous penetration depth. In (4*b*), ρ is the fluid density and μ is the fluid shear viscosity. The convention adopted for the Reynolds number is in line with Batchelor (1974) and is also referred to under alternate names such as the inverse Stokes or Womersley number. We note that the Reynolds number is often associated with the nonlinear convective inertial term of the Navier–Stokes equation. This latter convention has not been adopted here.

https://doi.org/10.1017/S0022112009993521 Published online by Cambridge University Press

Locally, at any point along the beam, the function $U(\bar{x}|\omega)$ can be expanded as

$$U(\bar{x}|\omega) = U_0 + A(\bar{x} - \bar{x}_0) + B(\bar{x} - \bar{x}_0)^2 + \cdots, \tag{5}$$

where

$$A = -\mathrm{i}\omega h_{fluid} \left.\frac{\mathrm{d}W}{\mathrm{d}x}\right|_{x=x_0}. \tag{6}$$

Importantly, since the length scale of the deflection function is the beam length L, it then follows that the quadratic term in (5) is $O(h_{fluid}/L)$ smaller than the linear term. Consequently, in the formal limit of $h_{fluid}/L \to 0$, which is implicitly specified in assumption (*a*), (5) becomes

$$U(\bar{x}|\omega) = U_0 + A(\bar{x} - \bar{x}_0) + O((h_{fluid}/L)^2),$$

which from (3) and (4*a*) gives the following expression for the beam velocity:

$$\boldsymbol{v} = U_0\hat{\boldsymbol{z}} + A\left(-\bar{z}\hat{\boldsymbol{x}} + (\bar{x} - \bar{x}_0)\,\hat{\boldsymbol{z}}\right). \tag{7}$$

We then solve the linearized Navier–Stokes equation in accordance with assumption (*e*),

$$\nabla\cdot\boldsymbol{v} = 0, \quad -\mathrm{i}\omega\rho\boldsymbol{v} = -\nabla P + \mu\nabla^2\boldsymbol{v}, \tag{8}$$

subject to the above boundary conditions, where $\boldsymbol{v}$ is the velocity field and P is the pressure. To begin, we note that the solution to the corresponding inviscid flow problem, satisfying the velocity components normal to the surfaces only (i.e. in the z direction), is

$$\boldsymbol{v}_{inv} = A\bar{z}\hat{\boldsymbol{x}} + (U_0 + A(\bar{x} - \bar{x}_0))\hat{\boldsymbol{z}}, \quad P = \mathrm{i}\rho\omega h_{fluid}(U_0 + A(\bar{x} - \bar{x}_0))\bar{z}. \tag{9}$$

However, this solution violates the velocity boundary conditions in the x direction at the channel walls. We therefore express the complete solution as the sum of this inviscid flow problem and a correction velocity in the x direction satisfying the continuity equation

$$\boldsymbol{v} = \boldsymbol{v}_{inv} + M(\bar{z})\hat{\boldsymbol{x}}. \tag{10}$$

Substituting (9) and (10) into (8) then yields the required governing equation and boundary conditions for $M(\bar{z})$

$$-\mathrm{i}\beta M = \frac{\mathrm{d}^2 M}{\mathrm{d}\bar{z}^2}, \quad M|_{\bar{z}=\pm 1/2} = \mp A, \tag{11}$$

for which the solution is

$$M(\bar{z}) = -A\frac{\sinh\left((1-\mathrm{i})\sqrt{\frac{\beta}{2}}\bar{z}\right)}{\sinh\left(\frac{1-\mathrm{i}}{2}\sqrt{\frac{\beta}{2}}\right)}. \tag{12}$$

Substituting (12) into (10) gives the required exact solution for the complete velocity field

$$\boldsymbol{v} = A\left(\bar{z} - \frac{\sinh\left((1-\mathrm{i})\sqrt{\frac{\beta}{2}}\bar{z}\right)}{\sinh\left(\frac{1-\mathrm{i}}{2}\sqrt{\frac{\beta}{2}}\right)}\right)\hat{\boldsymbol{x}} + (U_0 + A(\bar{x} - \bar{x}_0))\hat{\boldsymbol{z}}, \tag{13}$$

https://doi.org/10.1017/S0022112009993521 Published online by Cambridge University Press

where the pressure P remains unchanged from the inviscid flow result in (9) for arbitrary β. The rate-of-strain tensor can then be immediately calculated to give

$$\mathbf{e} = -\mathrm{i}\omega \left(1 - \frac{1-\mathrm{i}}{2}\sqrt{\frac{\beta}{2}} \frac{\cosh\left((1-\mathrm{i})\sqrt{\frac{\beta}{2}}\bar{z} \right)}{\sinh\left(\frac{1-\mathrm{i}}{2}\sqrt{\frac{\beta}{2}} \right)} \right) \left. \frac{\mathrm{d}W}{\mathrm{d}x} \right|_{x=x_0} (\hat{\boldsymbol{x}}\hat{\boldsymbol{z}} + \hat{\boldsymbol{z}}\hat{\boldsymbol{x}}). \tag{14}$$

The energy dissipated per cycle per unit volume in the fluid is obtained using (Batchelor 1974)

$$E_{diss/cycle/volume} = \frac{2\pi\mu}{\omega} \left(\mathbf{e} : \mathbf{e}^* - \frac{1}{3} |\mathrm{tr}\, \mathbf{e}|^2 \right), \tag{15}$$

where the asterisk (*) refers to the complex conjugate. Substituting (14) into (15), making use of the deflection function for the fundamental mode of a cantilever beam according to Euler–Bernoulli theory and integrating (15) over the volume of the fluid channel gives the energy dissipated per cycle in the fluid. Substituting this result into (1) gives the required expression for the quality factor

$$Q = F(\beta) \frac{\rho_{cant}}{\rho} \left(\frac{h_{cant}}{h_{fluid}} \right) \left(\frac{b_{cant}}{b_{fluid}} \right) \left(\frac{L}{h_{fluid}} \right)^2, \tag{16}$$

where, for the fundamental mode of vibration,

$$F(\beta) = 0.05379\beta \left(\int_{-1/2}^{1/2} \left| 1 - \frac{1-\mathrm{i}}{2}\sqrt{\frac{\beta}{2}} \frac{\cosh\left((1-\mathrm{i})\sqrt{\frac{\beta}{2}}s \right)}{\sinh\left(\frac{1-\mathrm{i}}{2}\sqrt{\frac{\beta}{2}} \right)} \right|^2 \mathrm{d}s \right)^{-1}, \tag{17}$$

and ρ_{cant} is the cantilever average density. Below, we consider the limits of small and large inertia to investigate the physical significance of this result.

2.1.1. *Small β limit*

We now consider the limit of small inertia ($\beta \ll 1$). The velocity field in this case is given by

$$\boldsymbol{v} = U_0\hat{\boldsymbol{z}} + A(-\bar{z}\hat{\boldsymbol{x}} + (\bar{x} - \bar{x}_0)\hat{\boldsymbol{z}}) + \beta\frac{\mathrm{Ai}}{12}(4\bar{z}^3 - \bar{z})\hat{\boldsymbol{x}} + O(\beta^2). \tag{18}$$

Physically, the first term in (18), $U_0\hat{\boldsymbol{z}}$, corresponds to the vertical rigid-body translation of the beam, the second term, $A(-\bar{z}\hat{\boldsymbol{x}} + (\bar{x} - \bar{x}_0)\hat{\boldsymbol{z}})$, corresponds to the rigid-body rotation and the third term corresponds to the leading-order effect due to fluid inertia. Note that if inertia is negligible ($\beta \to 0$), then the fluid undergoes a rigid-body displacement and rotation. Thus, energy dissipation is associated with non-zero inertial effects. This is discussed in § 3.

The rate-of-strain tensor can be evaluated directly from (15) and (18) to give

$$\mathbf{e} = \frac{1}{2}\omega\beta \left(\left(\frac{z}{h} \right)^2 - \frac{1}{12} \right) \left. \frac{\mathrm{d}W}{\mathrm{d}x} \right|_{x=x_0} (\hat{\boldsymbol{x}}\hat{\boldsymbol{z}} + \hat{\boldsymbol{z}}\hat{\boldsymbol{x}}) + O(\beta^2). \tag{19}$$

It then follows that the required asymptotic form for the function $F(\beta)$ defined in the quality factor, (16), is

$$F(\beta) = \frac{38.73}{\beta}, \quad \beta \ll 1. \tag{20}$$

https://doi.org/10.1017/S0022112009993521 Published online by Cambridge University Press

Equation (20) is the result we seek in the limit of small β, i.e. small fluid inertia. Below, we consider the opposite limit of large fluid inertia ($\beta \gg 1$).

2.1.2. *Large β limit*

In the limit of $\beta \to \infty$, flow in the channel is given by the corresponding inviscid flow problem (away from the surfaces). Applying the normal velocity boundary condition in figure 3(b) gives the required result for the velocity field in (9):

$$\boldsymbol{v} = A\bar{z}\hat{\boldsymbol{x}} + (U_0 + A(\bar{x} - \bar{x}_0))\hat{\boldsymbol{z}}. \tag{21}$$

Note that this results in a tangential flow (i.e. along the x direction) that is opposite in sign to the wall tangential velocities at $\bar{z} = \pm 1/2$; cf. (7) for the solid wall velocity with (21). As such, for large β there must exist a viscous boundary layer near each surface so that the complete boundary conditions at the surfaces are satisfied. The complete solution that accounts for the viscous boundary layers at $\bar{z} = \pm 1/2$ in this limit is obtained trivially from the exact solution in (13) to give

$$\boldsymbol{v} = A\left(\bar{z} - 2\exp\left(-\frac{1-\mathrm{i}}{2}\sqrt{\frac{\beta}{2}}\right)\sinh\left((1-\mathrm{i})\sqrt{\frac{\beta}{2}}\bar{z}\right)\right)\hat{\boldsymbol{x}} + (U_0 + A(\bar{x} - \bar{x}_0))\hat{\boldsymbol{z}}. \tag{22}$$

The rate-of-strain tensor can then be immediately calculated:

$$\boldsymbol{e} = -\mathrm{i}\omega\left(1 - (1-\mathrm{i})\sqrt{\frac{\beta}{2}}\exp\left(-\frac{1-\mathrm{i}}{2}\sqrt{\frac{\beta}{2}}\right)\cosh\left((1-\mathrm{i})\sqrt{\frac{\beta}{2}}\bar{z}\right)\right)\frac{\mathrm{d}W}{\mathrm{d}x}\bigg|_{x=x_0}(\hat{\boldsymbol{x}}\hat{\boldsymbol{z}} + \hat{\boldsymbol{z}}\hat{\boldsymbol{x}}). \tag{23}$$

Substituting (23) into (15), integrating the result over the fluid channel volume, neglecting all terms exponentially small in β and substituting the result into (1) gives the required expression for $F(\beta)$:

$$F(\beta) = 0.1521\sqrt{\beta}, \quad \beta \gg 1. \tag{24}$$

Equation (24) is the leading-order result in the asymptotic limit $\beta \gg 1$.

2.2. *Off-axis placement of channel*

We now turn our attention to investigating flow in the off-axis problem. To calculate the effect of off-axis channel placement, we consider the complete system that includes the channel inside the cantilever and the rigid channel leading into the cantilever; see figure 2. Consideration of the lead channel is imperative because the reference pressure is in the reservoir and not at the entrance to the actual cantilever. The length of the rigid lead channel is defined to be L_c, and the origin of the coordinate system is at the clamped end of the cantilever; see figures 1(a) and 2. A schematic of the off-axis flow problem is given in figure 3(c).

Importantly, this problem corresponds to extension and compression of a half-sealed channel, and therefore results in pumping of the fluid into and out of the lead channel/cantilever system. Because high pressures can be generated in such a configuration, we consider the case of viscous compressible flow. The governing equations in the time domain are

$$\frac{\partial \rho}{\partial t} + \rho\nabla\cdot\boldsymbol{v} = 0, \quad \rho\frac{\partial \boldsymbol{v}}{\partial t} = -\nabla P + \mu\nabla^2\boldsymbol{v} + \frac{1}{3}\mu\nabla(\nabla\cdot\boldsymbol{v}), \tag{25}$$

where the limit of small amplitude has been implicitly assumed (assumption (e)) and the Stokes hypothesis has been invoked, i.e. the bulk viscosity μ_B is set to zero. In

https://doi.org/10.1017/S0022112009993521 Published online by Cambridge University Press

this (linear) limit of small amplitude, the corresponding equation of state for the fluid is

$$\rho = \rho_0 + \rho_0 \kappa P, \tag{26}$$

where κ is the compressibility of the fluid and is related to the speed of sound c by $\kappa = 1/(\rho_0 c^2)$, and ρ_0 is the fluid density at ambient pressure ($P = 0$). Substituting (26) into (25), and noting the time ansatz used previously, gives

$$\boldsymbol{\nabla \cdot v} = \mathrm{i}\omega\kappa P, \quad -\mathrm{i}\omega\rho_0 \boldsymbol{v} = -\left(1 - \frac{1}{3}\mathrm{i}\mu\omega\kappa\right)\boldsymbol{\nabla} P + \mu\nabla^2 \boldsymbol{v}. \tag{27}$$

Importantly, as the channel walls move in the x direction, the total volume within the channel will vary. We therefore express the fluid velocity field $\boldsymbol{v}$ in terms of a reduced velocity $\boldsymbol{V}$ such that

$$\boldsymbol{v} = \boldsymbol{v}|_{x=L} + \boldsymbol{V}, \tag{28}$$

leading to zero reduced velocity at the free end of the cantilever. The boundary conditions at the channel walls for this reduced velocity $\boldsymbol{V}$ are then

$$\boldsymbol{V}|_{z=z_0 \pm h_{fluid}/2} = \begin{cases} \mathrm{i}\omega z_0 \left(\dfrac{\mathrm{d}W}{\mathrm{d}x} - \left.\dfrac{\mathrm{d}W}{\mathrm{d}x}\right|_{x=L}\right)\hat{\boldsymbol{x}} & : 0 \leqslant x \leqslant L, \\ -\mathrm{i}\omega z_0 \left.\dfrac{\mathrm{d}W}{\mathrm{d}x}\right|_{x=L} \hat{\boldsymbol{x}} & : -L_c \leqslant x < 0. \end{cases} \tag{29}$$

By ensuring the reduced velocity is zero at $x = L$, this approach inherently accounts for the effects of volume change in the channel: the reduced problem formally corresponds to a channel that is held fixed at its closed end, whose sidewalls are straining in their plane in an infinite fluid reservoir. The governing equation for this reduced problem is

$$\boldsymbol{\nabla \cdot V} = \mathrm{i}\omega\kappa P, -\mathrm{i}\omega\rho_0 \boldsymbol{V} = -\left(1 - \frac{1}{3}\mathrm{i}\mu\omega\kappa\right)\boldsymbol{\nabla} P + \mu\nabla^2 \boldsymbol{V} - \rho_0\omega^2 z_0 \left.\frac{\mathrm{d}W}{\mathrm{d}x}\right|_{x=L} \hat{\boldsymbol{x}}. \tag{30}$$

Because the cantilever length L greatly exceeds the channel thickness h_{fluid}, we scale the x coordinate by L and the z coordinate by h_{fluid}. We also choose the pressure scale appropriate for the *low inertia limit*, and the velocity scales from the boundary conditions and the continuity equation. This leads to the following set of scales:

$$x_s = L, \quad z_s = h_{fluid}, \quad u_s = \mathrm{i}\omega z_0 \left.\frac{\mathrm{d}W}{\mathrm{d}x}\right|_{x=L}, \quad w_s = \frac{h_{fluid}}{L} u_s, \quad P_s = \frac{\mu u_s L}{h_{fluid}^2}, \tag{31}$$

where the subscript s indicates a scaling. Note that the scaling for x differs from that used for the on-axis flow problem. Substituting (31) into (30) and noting that $L \gg h_{fluid}$ (assumptions (a) and (b)) gives the required leading-order scaled governing equations:

$$\frac{\partial \bar{u}}{\partial \bar{x}} + \frac{\partial \bar{w}}{\partial \bar{z}} = \mathrm{i}\alpha \bar{P}, \quad -\mathrm{i}\beta(1 + \bar{u}) = -\frac{\mathrm{d}\bar{P}}{\mathrm{d}\bar{x}} + \frac{\partial^2 \bar{u}}{\partial \bar{z}^2}, \tag{32}$$

where the velocity field $\boldsymbol{V} = u\hat{\boldsymbol{x}} + w\hat{\boldsymbol{z}}$, an overscore indicates a scaled variable, and the following dimensionless variables naturally arise:

$$\beta = \frac{\rho_0 \omega h_{fluid}^2}{\mu}, \quad \gamma = \left(\frac{\omega L}{c}\right)^2, \quad \alpha = \frac{\gamma}{\beta}. \tag{33}$$

https://doi.org/10.1017/S0022112009993521 Published online by Cambridge University Press

We emphasize that only two independent dimensionless parameters exist in the governing equations, and the third is a construct of these parameters; see (33). These three dimensionless parameters can be interpreted as follows:

(i) β is the squared ratio of the channel thickness to the viscous penetration depth and indicates the importance of *fluid inertia*. This corresponds to the *Reynolds number*, and is identical to the on-axis problem.

(ii) γ is the squared ratio of the cantilever length to the acoustic wavelength (multiplied by a constant) and indicates the importance of acoustic effects. This is termed the *normalized wavenumber*.

(iii) α is the ratio of γ and β and dictates when fluid compressibility significantly affects the flow due to *variations in fluid density* via the pressure. This is termed the *compressibility number* and is proportional to the dilation of a fluid element.

Note that (32) is correct to leading order for small h_{fluid}/L and also establishes that the pressure is independent of z in this limit. Importantly, the formal limit $h_{fluid}/L \to 0$ is consistent with Euler–Bernoulli beam theory and is therefore used throughout. It is also seen from (30) and (32) that fluid compressibility κ does not appear explicitly in the momentum equation within this lubrication limit. This establishes that use of the Stokes hypothesis is inconsequential here, and the bulk viscosity μ_B has no effect.

To solve (32), we search for a solution satisfying the continuity equation of the form

$$\bar{u}(\bar{x},\bar{z}) = f(\bar{x})k'(\bar{z}) + h(\bar{x}), \quad \bar{w}(\bar{x},\bar{z}) = -f'(\bar{x})k(\bar{z}), \tag{34}$$

where the functions $f(\bar{x})$, $h(\bar{x})$ and $k(\bar{z})$ are to be determined. Equation (34) makes use of the Helmholtz decomposition of a general vector field. Substituting (34) into (32) then gives

$$\frac{\mathrm{d}h}{\mathrm{d}\bar{x}} = \mathrm{i}\alpha\bar{P}, \quad \frac{\mathrm{d}\bar{P}}{\mathrm{d}\bar{x}} = Bf(\bar{x}) + \mathrm{i}\beta[1 + h(\bar{x})], \tag{35a}$$

$$k'''(\bar{z}) + \mathrm{i}\beta k'(\bar{z}) = B, \tag{35b}$$

$$f(\bar{x}) = S(\bar{x}) - h(\bar{x}), \tag{35c}$$

where B is a constant, and the boundary conditions for $k(\bar{z})$ are obtained by invoking the usual no-slip conditions at the channel walls

$$k\left(\pm\frac{1}{2}\right) = 0, \quad k'\left(\pm\frac{1}{2}\right) = 1, \tag{36}$$

where

$$S(\bar{x}) = \begin{cases} -1 + \dfrac{\dfrac{\mathrm{d}W}{\mathrm{d}\bar{x}}}{\dfrac{\mathrm{d}W}{\mathrm{d}\bar{x}}\Big|_{\bar{x}=1}} & : 0 \leqslant \bar{x} \leqslant 1, \\ -1 & : -\bar{L}_c \leqslant \bar{x} < 0. \end{cases} \tag{37}$$

Solving (35*b*) and (36) yields the solution for k,

$$k(\bar{z}) = \frac{\sinh\left((1-\mathrm{i})\sqrt{\dfrac{\beta}{2}}\bar{z}\right) - 2\bar{z}\sinh\left(\dfrac{1-\mathrm{i}}{2}\sqrt{\dfrac{\beta}{2}}\right)}{(1-\mathrm{i})\sqrt{\dfrac{\beta}{2}}\cosh\left(\dfrac{1-\mathrm{i}}{2}\sqrt{\dfrac{\beta}{2}}\right) - 2\sinh\left(\dfrac{1-\mathrm{i}}{2}\sqrt{\dfrac{\beta}{2}}\right)}, \tag{38a}$$

https://doi.org/10.1017/S0022112009993521 Published online by Cambridge University Press

and the constant B,

$$B = \frac{-2\mathrm{i}\beta \sinh\left(\dfrac{1-\mathrm{i}}{2}\sqrt{\dfrac{\beta}{2}}\right)}{(1-\mathrm{i})\sqrt{\dfrac{\beta}{2}}\cosh\left(\dfrac{1-\mathrm{i}}{2}\sqrt{\dfrac{\beta}{2}}\right) - 2\sinh\left(\dfrac{1-\mathrm{i}}{2}\sqrt{\dfrac{\beta}{2}}\right)}, \tag{38b}$$

where

$$\bar{z} = \frac{z - z_0}{h_{fluid}}. \tag{39}$$

Substituting (35c) into (34) then gives the required velocity field

$$\bar{u}(\bar{x},\bar{z}) = [S(\bar{x}) - h(\bar{x})]k'(\bar{z}) + h(\bar{x}), \quad \bar{w}(\bar{x},\bar{z}) = -[S'(\bar{x}) - h'(\bar{x})]k(\bar{z}), \tag{40}$$

where the governing equation for $h(\bar{x})$ is obtained from (35a) and (35c)

$$\frac{\mathrm{d}^2 h}{\mathrm{d}\bar{x}^2} + \alpha(\beta + \mathrm{i}B)h = \mathrm{i}\alpha B S(\bar{x}) - \alpha\beta. \tag{41}$$

The boundary conditions for (41) are then obtained by (i) ensuring that the pressure at the inlet to the channel ($\bar{x} = -\bar{L}_c$) equals the ambient pressure in the reservoir and (ii) the x component of the reduced velocity is zero at the free end of the cantilever ($\bar{x} = 1$):

$$h'(-\bar{L}_c) = h(1) = 0. \tag{42}$$

Note that there will be a slight pressure drop within the reservoir up to the inlet to the rigid lead channel at $\bar{x} = -\bar{L}_c$. However, in the limit $h_{fluid}/L \to 0$, this is negligible in comparison to the pressure drop over the channel length and is formally ignored to leading order.

The solution to (41) and (42) is easily evaluated using the Green's function method to yield

$$h(\bar{x}) = -\frac{\alpha}{M\cos[M(1+\bar{L}_c)]}\left\{\sin[M(1-\bar{x})]\int_{-\bar{L}_c}^{\bar{x}}[\mathrm{i}BS(x') - \beta]\cos[M(x'+\bar{L}_c)]\mathrm{d}x' + \cos[M(\bar{x}+\bar{L}_c)]\int_{\bar{x}}^{1}[\mathrm{i}BS(x') - \beta]\sin[M(1-x')]\mathrm{d}x'\right\}, \tag{43}$$

where

$$M = \sqrt{\alpha(\beta + \mathrm{i}B)}, \tag{44}$$

and the scaled pressure is obtained from (35a)

$$\bar{P} = \frac{1}{\mathrm{i}\alpha}\frac{\mathrm{d}h}{\mathrm{d}\bar{x}}. \tag{45}$$

The rate-of-strain tensor for this velocity field is

$$\boldsymbol{e} = \frac{\mathrm{i}\omega z_0}{2h_{fluid}}\left.\frac{\mathrm{d}W}{\mathrm{d}x}\right|_{x=L}[S(\bar{x}) - h(\bar{x})]k''(\bar{z})(\hat{\boldsymbol{x}}\hat{\boldsymbol{z}} + \hat{\boldsymbol{z}}\hat{\boldsymbol{x}}) + O\left(\frac{h_{fluid}}{L}\right). \tag{46}$$

2.2.1. *Incompressible flow ($\alpha \to 0$)*

We now examine the limit of incompressible flow. First, we note that the function $h(\bar{x}) = 0$ in this limit, and the reduced velocity field becomes

$$\bar{u}(\bar{x},\bar{z}) = S(\bar{x})k'(\bar{z}), \quad \bar{w}(\bar{x},\bar{z}) = -S'(\bar{x})k(\bar{z}). \tag{47}$$

https://doi.org/10.1017/S0022112009993521 Published online by Cambridge University Press

The corresponding expression for the scaled pressure gradient is

$$\frac{\mathrm{d}\bar{P}}{\mathrm{d}\bar{x}} = BS(\bar{x}) + \mathrm{i}\beta, \tag{48}$$

where $\bar{P}(-\bar{L}_c) = 0$ is the (ambient) inlet pressure condition.

The required solution for the velocity field $\boldsymbol{v}$ in the (original) inertial frame of reference of the cantilever is then obtained from (28), (31) and (40):

$$\boldsymbol{v} = \mathrm{i}\omega z_0 \left.\frac{\mathrm{d}W}{\mathrm{d}x}\right|_{x=L} \left\{ [1 + S(\bar{x})k'(\bar{z})]\hat{\boldsymbol{x}} - \frac{h_{fluid}}{L} S'(\bar{x})k(\bar{z})\hat{\boldsymbol{z}} \right\}. \tag{49}$$

Note that the z component of the velocity in (49) is $O(h_{fluid}/L)$ smaller than the x component, and hence negligible to leading order. Importantly, this analysis implicitly includes the lead channel of length L_c attached to the cantilever, and it is assumed that the entire lead channel/cantilever channel system is connected to an infinite fluid reservoir where the pressure is constant (to leading order).

2.2.2. *Compressible flow ($\alpha > 0$)*

Now, we examine the effects of compressibility on the flow within the channel. In this case, the velocity profile in the original inertial frame of reference is

$$\boldsymbol{v} = \frac{\mathrm{i}\omega z_0}{L} \left.\frac{\mathrm{d}W}{\mathrm{d}\bar{x}}\right|_{\bar{x}=1} \left\{ [1 + h(\bar{x}) + \{S(\bar{x}) - h(\bar{x})\}k'(\bar{z})]\hat{\boldsymbol{x}} - \frac{h_{fluid}}{L}[S'(\bar{x}) - h'(\bar{x})]k(\bar{z})\hat{\boldsymbol{z}} \right\}, \tag{50}$$

whereas the (unscaled) pressure is obtained from (31) and (45),

$$P = \rho_0 \omega^2 z_0 \left.\frac{\mathrm{d}W}{\mathrm{d}\bar{x}}\right|_{\bar{x}=1} \left(\frac{1}{\gamma} \frac{\mathrm{d}h}{\mathrm{d}\bar{x}} \right). \tag{51}$$

Note that the volume flux q entering the system is given by

$$q = \frac{\mathrm{i}\omega z_0 h_{fluid} b_{fluid}}{L} [1 + h(-\bar{L}_c)] \left.\frac{\mathrm{d}W}{\mathrm{d}\bar{x}}\right|_{\bar{x}=1}. \tag{52}$$

In the limit of infinite compressibility, from (37) and (41) we find

$$h(\bar{x}) = -1, \quad \alpha \to \infty, \tag{53}$$

and hence from (52) the volume flux W is zero, as expected.

2.3. *Complete flow within the fluid channel*

The complete flow field within the channel can now be calculated using the principle of linear superposition by adding the results for the on-axis and off-axis sub-problems. The total rate-of-strain tensor is obtained from (13) and (50):

$$\boldsymbol{e} = -\mathrm{i}\omega \left\{ \left(1 - \frac{1-\mathrm{i}}{2}\sqrt{\frac{\beta}{2}} \frac{\cosh\left((1-\mathrm{i})\sqrt{\frac{\beta}{2}}\bar{z}\right)}{\sinh\left(\frac{1-\mathrm{i}}{2}\sqrt{\frac{\beta}{2}}\right)} \right) \frac{\mathrm{d}W}{\mathrm{d}x} - \frac{z_0}{2h_{fluid}} \left.\frac{\mathrm{d}W}{\mathrm{d}x}\right|_{x=L} \times k''(z)[S(\bar{x}) - h(\bar{x})] \right\} (\hat{\boldsymbol{x}}\hat{\boldsymbol{z}} + \hat{\boldsymbol{z}}\hat{\boldsymbol{x}}). \tag{54}$$

https://doi.org/10.1017/S0022112009993521 Published online by Cambridge University Press

The quality factor can then be easily calculated using (15) to give

$$Q = F(\beta)\frac{\rho_{cant}}{\rho}\left(\frac{h_{cant}}{h_{fluid}}\right)\left(\frac{b_{cant}}{b_{fluid}}\right)\left(\frac{L}{h_{fluid}}\right)^2, \tag{55}$$

where, for an arbitrary mode of vibration described by W,

$$F(\beta) = \frac{\beta}{16\displaystyle\int_{-\bar{L}_c}^{1}\int_{-1/2}^{1/2}|G(X,Z)|^2\,\mathrm{d}Z\,\mathrm{d}X}, \tag{56a}$$

$$G(X,Z) = \left(1 - \frac{1-\mathrm{i}}{2}\sqrt{\frac{\beta}{2}}\frac{\cosh\left((1-\mathrm{i})\sqrt{\frac{\beta}{2}}Z\right)}{\sinh\left(\frac{1-\mathrm{i}}{2}\sqrt{\frac{\beta}{2}}\right)}\right)\frac{\mathrm{d}\bar{W}}{\mathrm{d}X} + \frac{\mathrm{i}\beta\bar{Z}_0}{2}$$
$$\times\left(\frac{\sinh\left((1-\mathrm{i})\sqrt{\frac{\beta}{2}}Z\right)}{(1-\mathrm{i})\sqrt{\frac{\beta}{2}}\cosh\left(\frac{1-\mathrm{i}}{2}\sqrt{\frac{\beta}{2}}\right) - 2\sinh\left(\frac{1-\mathrm{i}}{2}\sqrt{\frac{\beta}{2}}\right)}\right)[S(\bar{x}) - h(\bar{x})]\left.\frac{\mathrm{d}\bar{W}}{\mathrm{d}X}\right|_{X=1}, \tag{56b}$$

$$X = \frac{x}{L}, \quad Z = \frac{z - z_0}{h_{fluid}}, \quad \bar{Z}_0 = \frac{z_0}{h_{fluid}}, \tag{56c}$$

where $\bar{W}(X)$ is the normalized deflection function, such that $\bar{W}(1) = 1$. Equations (55) and (56) give the required result for the fluid channel embedded cantilever, which accounts for both on-axis and off-axis placement of the channel. The physical implications of this result will be explored in the next section together with a comparison to experimental measurements.

3. Results and discussion

We now examine the physical consequences of the above analysis and initially consider the case of on-axis placement of the channel. Throughout, we focus on the function $F(\beta)$ when discussing the quality factor Q, because these quantities are trivially related via the geometric and material properties of the cantilever/fluid system; see (55). The function $F(\beta)$ shall henceforth be termed the 'normalized quality factor'.

3.1. *On-axis flow problem*

A comparison of the asymptotic solutions for $F(\beta)$ in (20) and (24) and the exact solution in (16) is given in figure 4. Note that the exact solution follows the correct asymptotic behaviour in the limits of small and large Reynolds number β, as required. Interestingly, the quality factor exhibits a non-monotonic dependence on β: (i) for $\beta \ll 1$, the quality factor increases with decreasing β, whereas (ii) for $\beta \gg 1$, it increases with increasing β. The result is that the quality factor possesses a global minimum of $F = 1.8175$ at $\beta = 46.434$.

The physical origin of this unusual behaviour can be explained as follows. We begin by examining the limit of small inertia ($\beta \ll 1$), which exhibits the apparently counter-intuitive result that an enhancement in viscosity (reduction in β) reduces energy dissipation (increases the quality factor). In the formal limit of zero inertia, it

https://doi.org/10.1017/S0022112009993521 Published online by Cambridge University Press

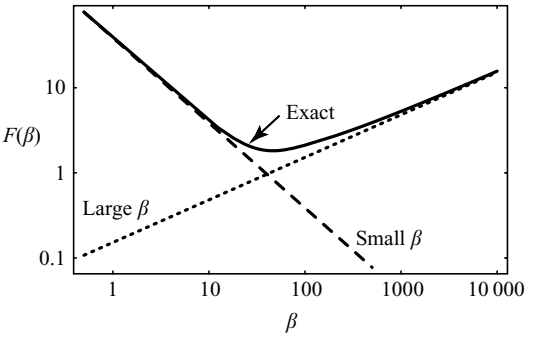


FIGURE 4. Plot of the normalized quality factor $F(\beta)$ for on-axis placement of the channel. Exact solution (see (16)), small β solution (see (20)) and large β solution (see (24)) are shown.

is seen from (18) that the fluid undergoes a rigid-body displacement and rotation. As such, the rate-of-strain tensor is zero and the fluid dissipates no energy. However, as inertia in the system increases (e.g. by either increasing the frequency of oscillation or decreasing the viscosity) the fluid cannot maintain its rigid-body behaviour and begins to drive a secondary flow that lags the primary rigid-body motion by 90°; see (18). This secondary flow exhibits non-zero rate-of-strain and therefore finite energy dissipation. The magnitude of this secondary flow increases with increasing inertia. Consequently, we find that inertia is the mechanism that drives energy dissipation in the low inertia limit: by increasing inertia we enhance the secondary flow and thus energy dissipation increases.

In the opposite limit of large inertia ($\beta \gg 1$), we find that energy dissipation rises (quality factor drops) with increasing viscosity (decreasing β). This is as one would expect intuitively and results from the presence of thin viscous boundary layers at the solid walls of the fluid channel. These thin boundary layers are identical to Stokes second problem, which dictates that an increase in viscosity increases the thickness of the viscous boundary layers and hence energy dissipation rises. The behaviour in the high inertia limit is therefore completely opposite to that for low inertia and leads immediately to the existence of a minimum in the quality factor (maximum in energy dissipation) at an intermediate value of inertia ($\beta = 46.434$).

Physically, the minimum in quality factor corresponds to merging of the viscous boundary layers as β is reduced, leading to a crossover from high inertia to low inertial flow. This establishes that the quality factor will decrease to a minimum and then increase, as the viscosity is systematically increased from the high inertia limit. This unique feature is of significant practical importance in developing ultra-sensitive devices through miniaturization, which is not found in conventional cantilevers immersed in fluid systems (Sader 1998). A brief discussion of higher-order effects that may manifest themselves in the ultra low inertia limit, which is relevant to miniaturization, is given below.

In passing, we remind the reader that the analysis presented has been derived in the formal limit where the channel width greatly exceeds the channel thickness. For completeness, an analysis of the on-axis problem for arbitrary channel aspect ratio is given in the Appendix. This shows that finite channel aspect ratio induces a relatively weak effect, with the above salient features of the quality factor preserved; see figure 23.

Before proceeding to the off-axis flow, it is pertinent to examine the effects of fluid compressibility on the on-axis problem. A scaling analysis reveals that compressibility

https://doi.org/10.1017/S0022112009993521 Published online by Cambridge University Press

will be important provided

$$\left(\frac{\omega L}{c}\right)^2 \left(\frac{h_{fluid}}{L}\right)^2 \sim O(1).$$

Clearly, this condition is violated in the formal limit $h_{fluid}/L \to 0$ at fixed L, which is implicitly assumed in the above analysis. Importantly, the condition is also violated in cantilevers used in practice (Burg *et al.* 2007). This, therefore, establishes that fluid compressibility is not important for the on-axis flow problem as has been assumed.

3.2. *Off-axis flow problem*

We now discuss the flow generated by off-axis placement of the channel. We consider the off-axis problem only, which ignores the contribution from the on-axis flow field.

3.2.1. *Incompressible flow*

To begin, we examine the singular case of incompressible flow, which corresponds to $\alpha \to 0$. In the limits of small and large fluid inertia, the velocity field in (49) becomes

$$\boldsymbol{v} = \mathrm{i}\omega z_0 \left.\frac{\mathrm{d}W}{\mathrm{d}x}\right|_{x=L} \hat{\boldsymbol{x}} \begin{cases} 1 + S(\bar{x})\left[6\left(\dfrac{z-z_0}{h_{fluid}}\right)^2 - \dfrac{1}{2}\right] & : \quad \beta \to 0 \\ 1 & : \quad \beta \to \infty \end{cases} + \; O\left(\frac{h_{fluid}}{L}\right). \tag{57}$$

Equation (57) establishes that the velocity field possesses a parabolic distribution across the channel thickness in the limit of small inertia ($\beta \ll 1$), as may be expected intuitively. In the opposite limit of high inertia ($\beta \gg 1$), the flow field away from the channel walls is plug flow, with fluid being pumped into and out of the channel in a rigid-body fashion. This is also expected, because the channel walls will generate thin viscous boundary layers in this limit allowing the fluid away from the walls to move synchronously with the end of the cantilever ($x = L$).

We now present numerical results for the flow field at finite inertia. Throughout, we consider the case where the length of the rigid lead channel equals the cantilever length, as in the practical case (Burg *et al.* 2007, 2009), i.e. $L_c = L$. In figure 5, results are given for the velocity profile distribution in the channel corresponding to the limits of small and large inertia. Note that the shear velocity gradient is greatest in the rigid lead channel, and decreases as it approaches the end of the cantilever ($x = L$), as expected. The corresponding results for the pressure are given in figure 6, where it is clear that the majority of the pressure drop (increase) occurs within the rigid lead channel for low inertia, whereas for high inertia the pressure drop is uniformly distributed over the entire channel.

3.2.2. *Compressible flow*

Next, we include the effects of compressibility and study how this modifies the flow field. We again consider the practical case where the length of the rigid lead channel equals the cantilever length, i.e. $L_c = L$. Note that practical cantilevers have a compressibility number α that lies in the range $0.01 < \alpha < 1$.

Figure 7 illustrates the effects of fluid compressibility on the velocity field for moderately small inertia $\beta = 10$. Note that compressibility can profoundly affect the velocity field. A slight increase in compressibility, from the incompressible limit, leads to a significant increase in fluid velocity entering the channel; see bottom-most traces in figures 7(*a*)–7(*e*). Interestingly, as compressibility is increased further, a maximum velocity is obtained (figure 7*c*) which then subsequently decreases.

https://doi.org/10.1017/S0022112009993521 Published online by Cambridge University Press

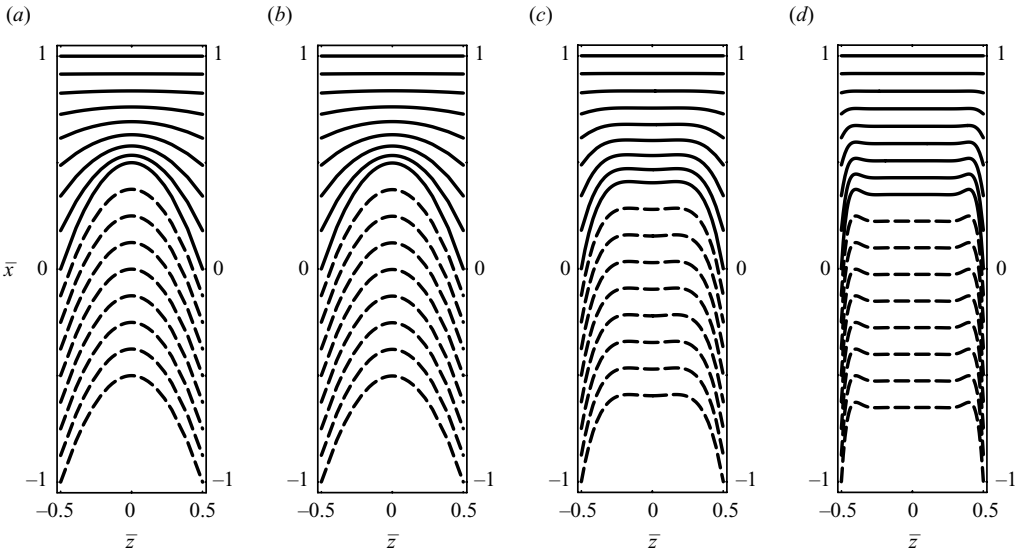


FIGURE 5. Velocity profile (magnitude) within the rigid channel/cantilever system. Variation in fluid velocity relative to wall velocity for $\bar{x} \in [-1, 1]$ and $\Delta\bar{x} = 0.125$. Notes: $\bar{x} = 0$ corresponds to the clamped end of the cantilever. Velocity is scaled differently in rigid lead channel and cantilever, for presentation only. (*a*) $\beta = 0.0001$, (*b*) $\beta = 10$, (*c*) $\beta = 100$, (*d*) $\beta = 1000$.

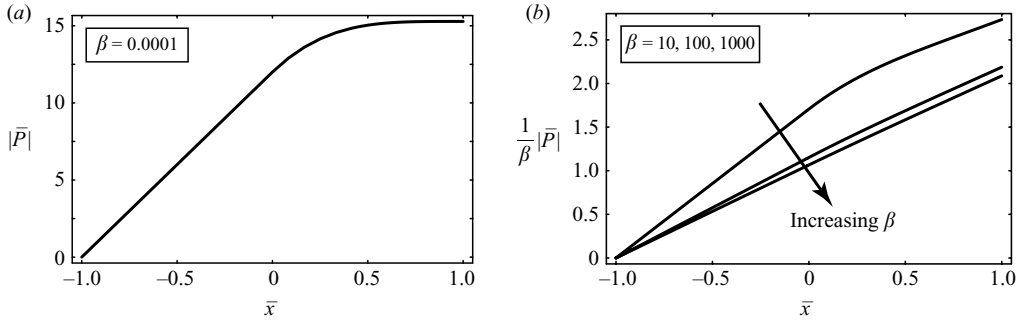


FIGURE 6. Normalized pressure profile $\bar{P}$ (magnitude of (48)) within the rigid channel/cantilever system. Pressure scale used is $P_s = \mu u_s L / h_{fluid}^2$ and is appropriate for the low inertia incompressible limit, i.e. $\beta \ll 1$ and $\alpha \ll 1$; see (31). (*a*) $\beta = 0.0001$, (*b*) $\beta = 10$, $\beta = 100$, $\beta = 1000$.

To investigate the origin of this behaviour, we present results for the volumetric flow rate entering the rigid lead channel in figure 8 as a function of the acoustic wavenumber γ, for a range of Reynolds numbers β. We remind the reader that $\alpha = \gamma/\beta$. For low inertia $\beta = 1$ (high viscous damping), the volumetric flux is seen to decrease monotonically with increasing compressibility. However, as damping is systematically reduced, by increasing β, this monotonicity in the volume flux disappears and is replaced with clear resonance behaviour. This explains the increase in fluid velocity observed in figure 7, which is due to the fundamental acoustic resonance of the cantilever/rigid lead channel system, which occurs at $\alpha\beta = \gamma = 0.28$ for $\beta = 10$.

https://doi.org/10.1017/S0022112009993521 Published online by Cambridge University Press

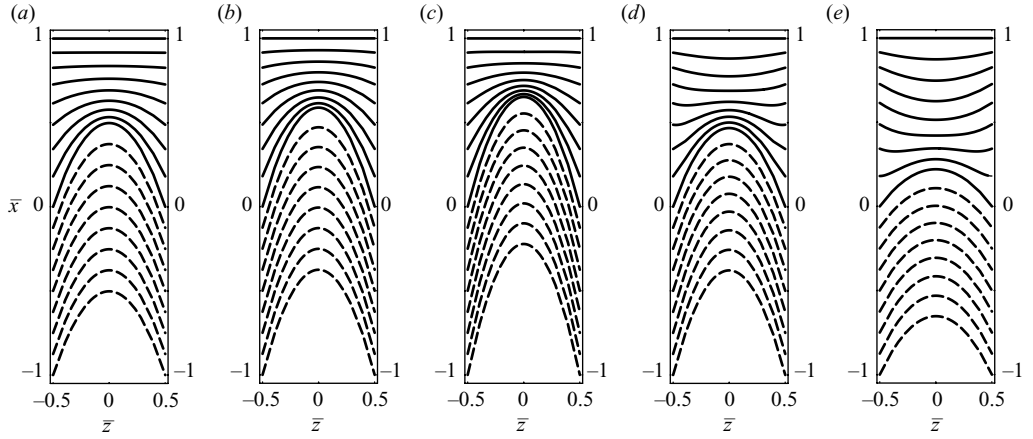


FIGURE 7. Velocity profile (magnitude) within the rigid channel/cantilever system showing effects of compressibility. Variation in fluid velocity relative to wall velocity for $\bar{x} \in [-1, 1]$ and $\Delta\bar{x} = 0.125$. Note: $\bar{x} = 0$ corresponds to the clamped end of the cantilever. Moderately low inertia: $\beta = 10$. (*a*) $\alpha = 0$, (*b*) $\alpha = 0.01$, (*c*) $\alpha = 0.03$, (*d*) $\alpha = 0.05$, (*e*) $\alpha = 0.1$.

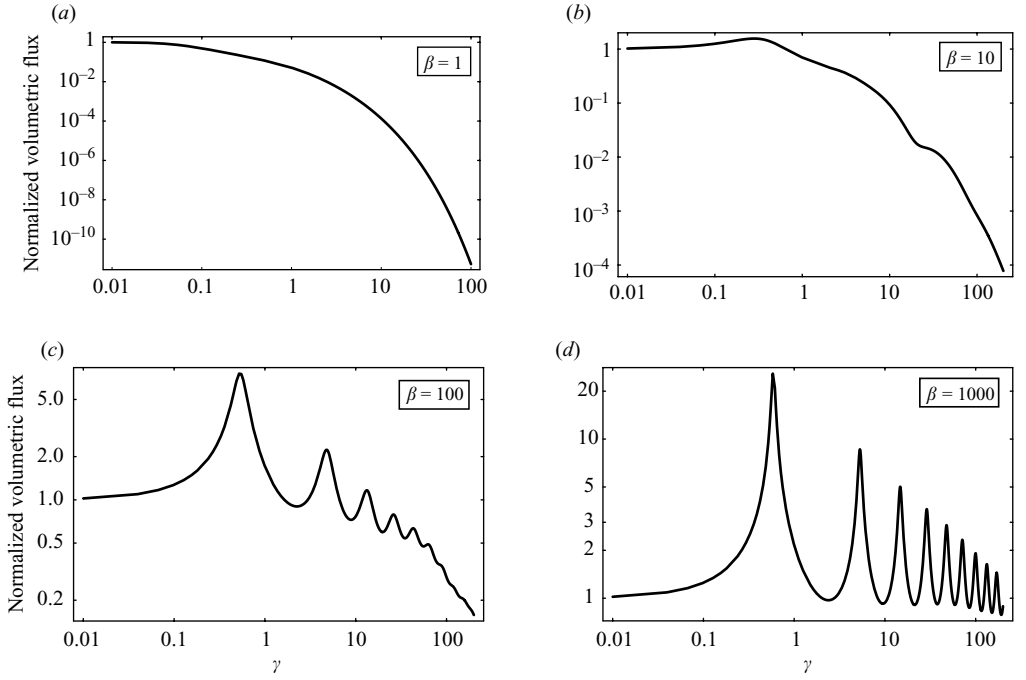


FIGURE 8. Normalized magnitude of volumetric flux into rigid lead channel as a function of the normalized wavenumber γ. (*a*) $\beta = 1$, (*b*) $\beta = 10$, (*c*) $\beta = 100$, (*d*) $\beta = 1000$. Volumetric flux scale is $q_s = u_s h_{fluid} b_{fluid}$.

Note that this resonance behaviour is strongly dependent on β, and for low β the system can become overdamped, leading to no observed resonance. Indeed, it is found that for fixed β, the number of resonances is finite, with the system becoming increasingly damped with increasing mode number, e.g. see figure 8(*c*), where only six resonance peaks are present for all γ.

https://doi.org/10.1017/S0022112009993521 Published online by Cambridge University Press

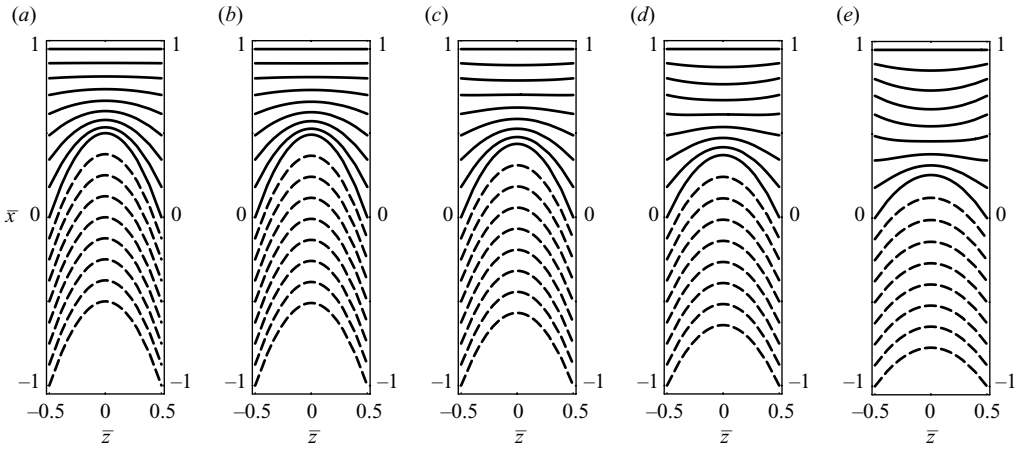


FIGURE 9. Velocity profile within the rigid channel/cantilever system showing effects of compressibility. Variation in fluid velocity relative to wall velocity for $\bar{x} \in [-1, 1]$ and $\Delta\bar{x} = 0.125$. Note: $\bar{x} = 0$ corresponds to the clamped end of the cantilever. Low inertia: $\beta = 0.0001$. (*a*) $\alpha = 0$, (*b*) $\alpha = 0.01$, (*c*) $\alpha = 0.03$, (*d*) $\alpha = 0.05$, (*e*) $\alpha = 0.1$.

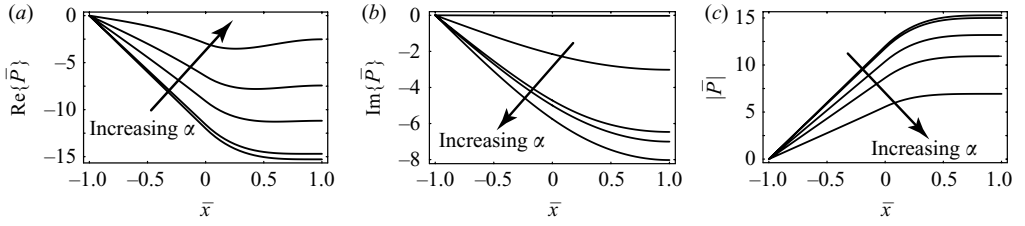


FIGURE 10. Normalized pressure profile $\bar{P}$ within the rigid channel/cantilever system showing effects of compressibility. Pressure scale used is $P_s = \mu u_s L / h_{fluid}^2$ and is appropriate for the low inertia limit, i.e. $\beta \ll 1$ and $\alpha \ll 1$; see (31). Low inertia: $\beta = 0.0001$. $\alpha = 0.0001$, 0.01, 0.03, 0.05, 0.1. (*a*) Real (in-phase with wall velocity) component; (*b*) imaginary (out-of-phase with wall velocity) component; (*c*) absolute value.

To further illustrate the above-described damping effect, figure 9 presents results for the velocity field at very low inertia $\beta = 0.0001$, for which no resonance behaviour is observed; in contrast to the results presented in figure 7 (for moderately small inertia), the magnitude of velocity at the channel entrance ($\bar{x} = -1$) decreases monotonically with α. The corresponding pressure profile throughout the channel is given in figure 10. Note that as compressibility is increased, i.e. α increases, the dissipative (real) component of the scaled pressure decreases in magnitude. For $\alpha \geqslant 0.03$, the pressure gradient reverses sign, which drives the flow in the opposite direction. This feature is manifested in figure 9. We thus find that the fluid velocity relative to the wall moves in the opposite direction near the free end of the cantilever to that in the rigid channel. In contrast, the inertial (imaginary) component of the pressure increases with increasing α due to the increased elasticity of the fluid system. The overall effect of compressibility is to reduce the magnitude of the pressure drop leading to lower volumetric flux into the cantilever.

Although the above variations in parameter space serve to illustrate the dominant effects of compressibility, through the compressibility number α, they are difficult to realize experimentally since this would require fluids with different speeds of sound.

https://doi.org/10.1017/S0022112009993521 Published online by Cambridge University Press

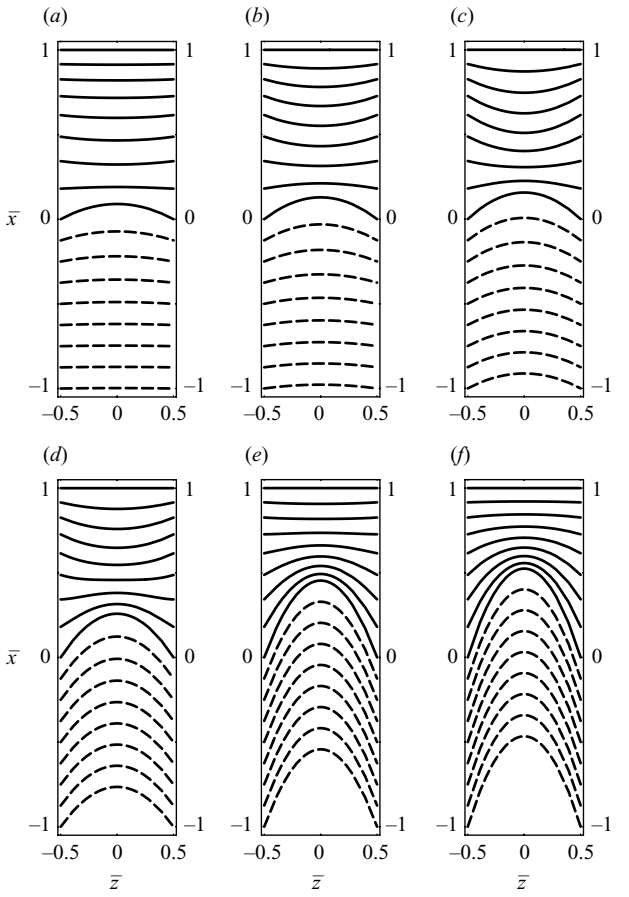


FIGURE 11. Velocity profile within the rigid channel/cantilever system as viscosity is varied for fixed fluid density. Variation in fluid velocity relative to wall velocity for $\bar{x} \in [-1, 1]$ and $\Delta\bar{x} = 0.125$. Note: $\bar{x} = 0$ corresponds to the clamped end of the cantilever. $\gamma = 0.03$. Increasing β from left to right. (*a*) $\beta = 0.01$, (*b*) $\beta = 0.03$, (*c*) $\beta = 0.1$, (*d*) $\beta = 0.3$, (*e*) $\beta = 1$, (*f*) $\beta = 10$.

An alternative approach to enhance the effects of compressibility is to increase the viscosity while holding the speed of sound and density of the fluid constant. This is easily achieved in practice, because the speed of sound of most liquids is comparable. In this case, γ is fixed and β (and hence $\alpha = \gamma/\beta$) changes as the viscosity varies. We consider the typical case where $\gamma = 0.03$ (which is identical to the 3 μm channel thickness cantilever investigated in § 3.4). Figure 11 shows the velocity profile in the entire channel system under these conditions.

Note that increasing viscosity corresponds to decreasing β. The effects of fluid compressibility are clear in figure 11 and demonstrate that they can profoundly influence the flow. The results for $\beta = 1$ and $\beta = 10$ are essentially the incompressible solution for low β exhibiting parabolic velocity profiles. However, as the viscosity increases (β decreases), the pressure also increases and ultimately becomes large enough to significantly compress the fluid. This reduces the volumetric flow rate into the channel system since the fluid is able to intrinsically accommodate the volume variations in the cantilever as it oscillates. We also note that flow reversal becomes

https://doi.org/10.1017/S0022112009993521 Published online by Cambridge University Press

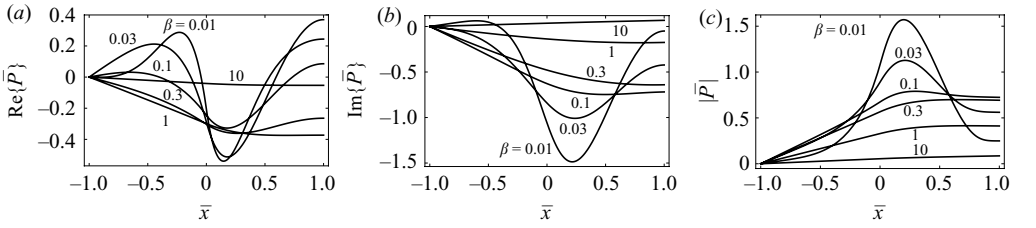


FIGURE 12. Normalized pressure profile $\bar{P}$ within the rigid channel/cantilever system showing effects of compressibility. Pressure scale used is $P_s = \mu u_s L/h_{fluid}^2/\alpha$ and is appropriate for the low inertia compressible limit, i.e. $\beta \ll 1$ and $\alpha = \gamma/\beta \gg 1$. Resonator parameters: $\gamma = 0.03$. $\beta = 0.01, 0.03, 0.1, 0.3, 1, 10$. Pressure variation increases with decreasing β. (*a*) Real (in-phase with wall velocity) component; (*b*) imaginary (out-of-phase with wall velocity) component; (*c*) absolute value.

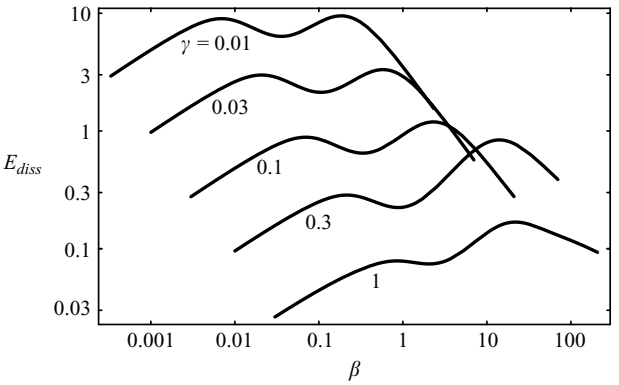


FIGURE 13. Normalized rate of total energy dissipation per unit cycle for various $\gamma = 0.01, 0.03, 0.1, 0.3, 1$. Observed maxima shift to right in β space with increasing γ in accord with resonance condition $\alpha = \gamma/\beta \sim O(1)$. Energy scale is $E_s = 4\pi\rho_0 L b_{fluid} h_{fluid} |u_s|^2$.

present in the flow and the shear velocity gradients decrease in magnitude as a result of compressibility.

The velocity variations as a function of viscosity in figure 11 can be understood through an examination of the pressure distribution in the fluid channel/cantilever system. Figure 12 shows the (scaled) pressure variation in the whole channel system under the conditions specified in figure 11; the pressure scaling differs from that used in figure 10. Note the correlation between the real component of the pressure (in-phase with the wall velocity) and the velocity behaviour in the fluid. As the effects of compressibility increase (β decreases), the real component of the pressure and pressure gradient change sign, and this drives the flow in alternate directions. Interestingly, the magnitude of this component is approximately independent of β, for $\beta \leqslant 1$. In contrast, the magnitude of the imaginary component (out-of-phase with the wall velocity) and the total magnitude of the pressure increase with decreasing β.

3.2.3. *Energy dissipation*

In figure 13 we present results for the (scaled) rate of energy dissipation in the channel due to off-axis flow for $\gamma \in [0.01, 1]$. Note that $\alpha = \gamma/\beta$, and hence increasing β reduces the effects of compressibility; see (32). In the limit of large inertia ($\beta \gg 1$), we find that the energy dissipated *decreases with increasing* β, as is expected for

https://doi.org/10.1017/S0022112009993521 Published online by Cambridge University Press

incompressible flow; increasing β can be easily achieved in practice by reducing the viscosity while holding the density constant. However, in the asymptotic limit $\beta \ll 1$, the energy dissipated *decreases with decreasing* β; see § 3.5 for a discussion of higher-order mechanisms at small β that are not included in the present model. This latter phenomenon is due to the increasing effects of compressibility that limit the volume flux into the channel and hence reduce the rate-of-strain as illustrated in figure 11. In the intermediate regime $\alpha = \gamma/\beta \sim O(1)$, we find that energy dissipation features two maxima, with a local minimum between these peaks. The mechanism for this behaviour arises from competing dissipative effects in the rigid lead channel and the cantilever proper, as we now discuss.

Rigid lead channel ($x < 0$). To begin, we focus on the rigid lead channel and consider the asymptotic limit of incompressible flow $\alpha \ll 1$, which corresponds to $\beta \gg 1$ at fixed γ. As viscosity increases in the high inertia limit, the Reynolds number β decreases whereas the normalized acoustic number γ remains fixed. In this incompressible limit, energy dissipation rises with increasing viscosity. However, the pressure also rises simultaneously and ultimately reaches a level where it can significantly compress the fluid. This reduces the shear velocity gradients, which in turn reduces energy dissipation. Energy dissipation ultimately approaches zero with increasing viscosity. These competing effects lead to the overall feature of an enhancement of energy dissipation at high inertia, and a reduction at low inertia as the viscosity increases (β decreases). This in turn explains the existence of a maximum in energy dissipation at intermediate β.

Cantilever proper ($x > 0$). We now examine energy dissipation in the cantilever proper. Unlike the rigid lead channel, the peak in energy dissipation does not occur at the transition point from incompressible to compressible flow, but is due to a peak in flow reversal that results from compressibility effects. To understand this, we note that as viscosity increases, the pressure rises high enough to significantly compress the flow and this leads to reversal in the pressure gradient. This in turn results in flow reversal in this region (see figures 11 and 12) and thus a reversal in the sign of the shear velocity gradients. Importantly, in the limit of infinite compressibility, the shear velocity gradients are zero. As such, there must exist an intermediate value of viscosity that leads to a maximum in the reversed flow velocity and hence a maximum in energy dissipation. This salient feature explains the existence of maximum energy dissipation at intermediate values of β for this region ($x > 0$). In general, this critical value of β differs from that for the rigid lead channel discussed above. This shift in the position of the maximum in the cantilever proper explains the double humped feature in figure 13, which is obtained by superimposing the energy dissipation in the cantilever proper ($x > 0$) and rigid lead channel ($x < 0$). The distribution of energy dissipation throughout the cantilever/rigid channel system shown in figure 14 reveals that the rightmost maximum in β space is due to the rigid lead channel, whereas the leftmost maximum is due to the cantilever proper. Variation in the shape of the total energy dissipation curves in figure 13 for increasing γ is due to the increasing effects of fluid inertia at large values of β.

The competing compressibility effects in the rigid lead channel and cantilever proper, which lead to maxima at different values of β, thus give rise to a local minimum in the energy dissipated at intermediate values of β. Importantly, the above discussion establishes that the rightmost maximum in β space results from enhancement in the magnitude of the pressure, whereas the leftmost maximum is caused by the pressure gradient (not the magnitude of the pressure). This feature allows for tuning of the positions of these two maxima in β space, by appropriate adjustment of the dimensions of the cantilever/lead channel system. As such, the β

https://doi.org/10.1017/S0022112009993521 Published online by Cambridge University Press

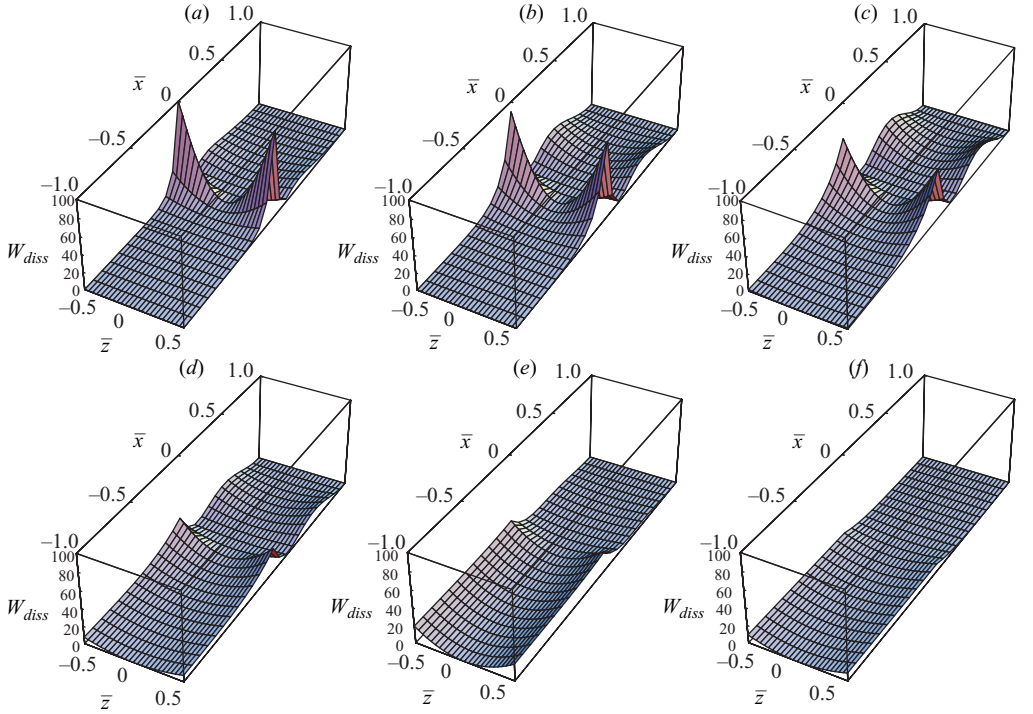


FIGURE 14. Normalized rate of energy dissipation distribution (per unit volume) for $\gamma = 0.01$ and increasing $\beta = 0.001, 0.003, 0.01, 0.03, 0.1, 1$ (*a–f*). Energy (per unit volume) scale is $W_s = 4\pi\rho_0 |u_s|^2$.

distance between the observed local maxima in energy dissipation will depend on the ratio of the cantilever length L to that of the rigid lead channel L_c. This feature is illustrated in figure 15. Note that the position of the leftmost maximum is independent of L_c/L (at fixed cantilever length L), as expected, because this arises from flow in the cantilever proper ($x > 0$). The rightmost maximum, however, depends strongly on L_c/L, because by changing the length L_c of the rigid lead channel, its contribution to the total energy dissipation is enhanced or reduced. By increasing the length of the rigid channel L_c, the position of the rightmost maximum occurs at higher values of β, because this enhances the pressure in that region leading to an earlier onset of compressibility effects. Thus, increasing the rigid channel length amplifies the effect of compressibility as expected. The enhanced topmost curve in figure 15 results from strong overlap in the flow within the cantilever proper and rigid channel, due to a short rigid lead channel.

Maximum pressure. We continue our discussion of the off-axis flow problem by examining the maximum pressure generated in the fluid channel. The pressure in various practical flow regimes scales in the following manner with respect to the explicit cantilever and fluid properties:

$$P \sim \begin{cases} \mu\omega \left(\dfrac{z_0}{h_{fluid}}\right)\left(\dfrac{a}{h_{fluid}}\right) : & \beta \ll 1, \alpha \ll 1 \text{ (low inertia, incompressible)}, \\ \rho_0\omega^2 z_0 a : & \beta \gg 1, \gamma \ll 1 \text{ (high inertia, incompressible)}, \\ \rho_0 c^2 \left(\dfrac{z_0}{L}\right)\left(\dfrac{a}{L}\right) : & \beta \ll 1, \alpha \gg 1 \text{ (low inertia, compressible)}, \end{cases} \tag{58}$$

https://doi.org/10.1017/S0022112009993521 Published online by Cambridge University Press

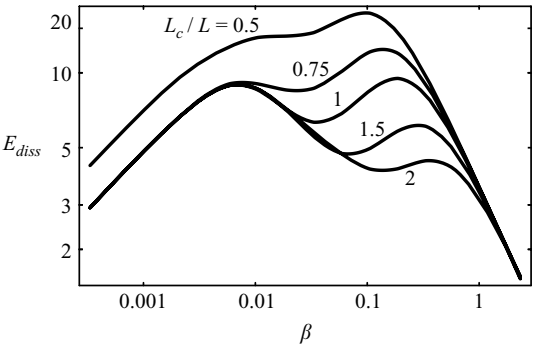


FIGURE 15. Normalized rate of total energy dissipation for $\gamma = 0.01$ and various ratios $L_c/L = 0.5, 0.75, 1, 1.5, 2$. L_c/L increases from top to bottom curves. Energy scale is the same as in figure 13.

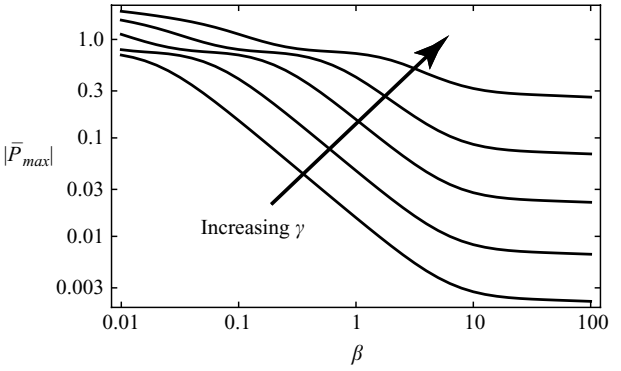


FIGURE 16. Magnitude of normalized maximum pressure $|\bar{P}_{max}|$ within the rigid channel/cantilever system for various normalized acoustic numbers $\gamma = 0.001, 0.003, 0.01, 0.03, 0.1$. Pressure scale is $P_s = \rho_0 c^2 u_s/(\omega L)$ and is appropriate for the low inertia compressible limit, i.e. $\beta \ll 1$ and $\alpha \gg 1$; see (58). Length of the rigid lead channel equals the cantilever length, i.e. $L_c = L$.

where a is the amplitude of oscillation. Note that numerical factors are ignored in (58). From (58), we see that increasing the oscillation amplitude, a, and off-axis placement, z_0, of the fluid channel always enhances the maximum pressure, as required. Figure 16 gives results for the magnitude of the maximum normalized pressure in the fluid channel as a function of fluid inertia and compressibility. The pressure scale in the low inertia compressible limit ($\beta \ll 1, \alpha \gg 1$) is used throughout, because this does not change as the cantilever is (i) uniformly reduced in size, nor (ii) as the fluid viscosity is varied. Both situations are considered below.

From figure 16, we observe that as the fluid viscosity is increased (β decreases), the maximum pressure also increases as expected. This is particularly pronounced in the low inertia regime ($\beta < O(1)$) where the viscous boundary layers generated at the surfaces strongly overlap. In the limit of very low inertia ($\beta \ll 1$), the pressure is high enough to induce significant dilation of the fluid, and this relaxes the monotonic increase in pressure as viscosity is increased note that the normalized maximum pressures are of order unity in this limit, as required by the pressure scale chosen.

Next, we examine the effects of miniaturization on the maximum pressure. From (33) we find that as the cantilever geometry is *uniformly reduced in size*, the characteristic

https://doi.org/10.1017/S0022112009993521 Published online by Cambridge University Press

dimensionless parameters for the flow vary according to the following scaling relations:

$$\beta \sim h_{cant}\left(\frac{h_{fluid}}{L}\right)^2, \quad \gamma \sim \left(\frac{h_{cant}}{L}\right)^2, \quad \alpha \sim \frac{1}{h_{fluid}}\left(\frac{h_{cant}}{h_{fluid}}\right). \tag{59}$$

From these relations it is clear that the effects of compressibility are enhanced as the cantilever is miniaturized (α increases), while the effects of fluid inertia are reduced (β decreases). In contrast, the normalized wavenumber γ remains constant throughout, indicating that the acoustic properties of the flow are unperturbed by miniaturization. From figure 16, it follows that miniaturization, which results in a reduction in β at constant γ, will in turn enhance the maximum pressure in the device.

Cavitation. Using the results presented in figure 16 for the off-axis flow maximum pressure, we now assess the possibility of inducing cavitation in the fluid channel. This is expected to occur when the maximum (negative) pressure, generated by the cantilever oscillation, decreases the ambient pressure below the vapour pressure of the liquid contained in the channel; see Batchelor (1974) for further discussion. Since the vapour pressure of water and glycerol at room temperature is well below 1 atm (∼100 kPa), this requires the maximum pressure to be comparable to 1 atm.

We note that pressure due to the on-axis flow scales as $\rho_0\omega^2 h_{fluid}a$, and is always given by the inviscid flow result in (9). Significant pressures can also be generated by the on-axis flow, but are normally smaller than those that can be generated by the off-axis flow. The effects of on-axis flow are thus not considered here.

For the purpose of illustration, we consider one of the cantilevers studied by Burg *et al.* (2009); see cantilever B in § 3.4, where its dimensions are listed. We assume a typical oscillation amplitude of $a = 100$ nm throughout. For water, the dimensionless parameters are $\beta = 12$ and $\gamma = 0.035$, and a maximum pressure of $2.1(z_0/h_{fluid})$ kPa is obtained, where z_0 is the off-axis placement of the fluid channel as specified above. Note that the maximum off-axis placement in any device is $z_0 = (h_{cant} - h_{fluid})/2$; for this cantilever device $(z_0/h_{fluid})_{max} = 2/3$. Therefore, regardless of the choice of off-axis placement, the maximum pressure induced in water is well below the pressure required to achieve cavitation. Using pure glycerol, we find $\beta = 0.010$ and $\gamma = 0.023$, and a maximum pressure of $47(z_0/h_{fluid})$ kPa. Therefore, even if the fluid channel is placed as far as possible from the neutral axis of the beam, i.e. z_0/h_{fluid} is maximized, pressures in excess of 1 atm in glycerol are not predicted to be possible. Therefore, current devices are thus not prone to these effects.

From (58), it is clear that to increase the maximum pressure, the cantilever must be made shorter (thus increasing the resonant frequency), and the off-axis channel position z_0 and oscillation amplitude a increased.

If the length L of cantilever B is reduced to 100 μm, while keeping all other dimensions identical, the picture changes dramatically. Using water, the dimensionless parameters are $\beta = 54$ and $\gamma = 0.16$, and the maximum pressure becomes $47(z_0/h_{fluid})$ kPa. Since the maximum off-axis placement in this device is $(z_0/h_{fluid})_{max} = 2/3$, the maximum possible pressure is 31 kPa, which is approximately a third that required to induce cavitation. However, using pure glycerol, we obtain $\beta = 0.045$ and $\gamma = 0.10$, and a maximum pressure of $210(z_0/h_{fluid})$ kPa; cavitation is therefore possible in this latter case.

Further reduction in length to 50 μm yields $1900(z_0/h_{fluid})$ kPa and $840(z_0/h_{fluid})$ kPa in water and pure glycerol, respectively. As such, even a small off-axis placement

https://doi.org/10.1017/S0022112009993521 Published online by Cambridge University Press

of the fluid channel is predicted to allow for cavitation in both water and pure glycerol.

Finally, we note that the model implicitly assumes that fluid density variations due to compressibility are small, allowing for linearization of the governing equations and equation of state. Pressures in the vicinity of 1 atm induce density variations of less than 0.01 %. Thus, the underlying model assumptions remain intact when exploring the *onset* of cavitation. Once cavitation is achieved, however, the continuum approximation breaks down and applicability of the model must be drawn into question.

3.3. *Complete flow*

We now combine the flow fields for the on-axis and off-axis problems to obtain the complete flow for the cantilever/rigid lead channel system. To begin, we examine the limiting case of incompressible flow and study the energy dissipation in the system.

3.3.1. *Incompressible flow*

We again focus on the normalized quality factor $F(\beta)$. In the limits of small and large inertia, the asymptotic behaviour of this function for the fundamental mode of vibration can be explicitly derived from the exact solution

$$F(\beta) = \begin{cases} \dfrac{38.73\beta}{\beta^2 + 564.6\bar{Z}_0^2\left(1 + \dfrac{\beta^2}{8400}\right)} & : \quad \beta \to 0, \\ \dfrac{\sqrt{\beta}}{6.573 + 1.718\bar{Z}_0^2} & : \quad \beta \to \infty. \end{cases} \tag{60}$$

Equation (60) clearly demonstrates that off-axis placement of the channel can exert a strong influence on the quality factor. The overall effect as the viscosity is varied will now be described. We restrict ourselves to the case where the off-axis position of the channel $\bar{Z}_0$ is non-zero and significantly less than one channel thickness, i.e. $\bar{Z}_0 \ll 1$, which is the practical case commonly encountered. Note that decreasing the viscosity (at constant density) will increase β.

Starting in the low inertial limit, we observe from (60) that the quality factor will increase with increasing β, i.e. decreasing viscosity. In this regime, oscillatory inflow/outflow within the channel, due to off-axis placement, dominates the inertial mechanism for dissipation previously described for on-axis channels. Importantly, this additional flow has a non-zero effect in the limit of zero fluid inertia, which gives rise to a strong deviation from the on-axis result in the limit as $\beta \to 0$. This behaviour is present for $\beta < \beta_{max}$, where

$$\beta_{max} = 23.76\bar{Z}_0 + O\left(\bar{Z}_0^2\right). \tag{61}$$

Note that this asymptotic formula is a good approximation for $\bar{Z}_0 < 0.5$, exhibiting a maximum error of 14 %.

At the critical point ($\beta = \beta_{max}$), the quality factor attains a local maximum value. Importantly, for off-axis positions significantly less than one channel thickness ($\bar{Z}_0 \ll 1$), this critical value for β is smaller than that required for the minimum quality factor predicted by (31), i.e. $\beta_{min} = 46.434$. Consequently, increasing β further will decrease the quality factor, with the inertial mechanism previously described for on-axis flow dominating the inflow/outflow in the channel, until a minimum quality factor is reached at $\beta_{min} = 46.434$. Further increase in β will then enhance the quality factor as before. These salient features of the quality factor are illustrated in figure 17.

https://doi.org/10.1017/S0022112009993521 Published online by Cambridge University Press

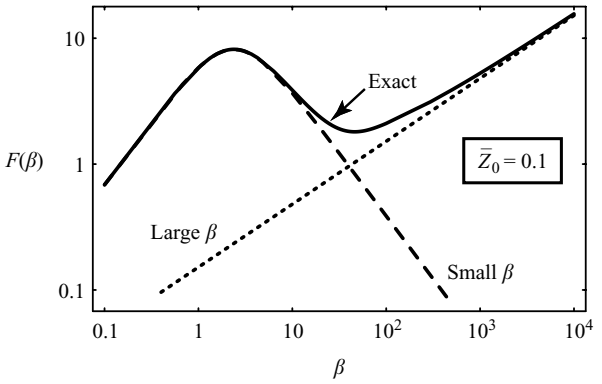


FIGURE 17. Plot of $F(\beta)$ function for quality factor. Exact solution (see (56*a*)), small β solution (see (60)) and large β solution (see (60)) are shown. Results for off-axis placement: $\bar{Z}_0 = 0.1$.

The results in figure 17 for the case of off-axis placement are to be compared with those in figure 4 for on-axis placement. Note that the dominant features of the quality factor profile are accurately predicted by the asymptotic results in figure 17. We also observe that off-axis placement dominates the behaviour only for low inertia, i.e. small β.

Importantly, the above-described turnover in the quality factor (see figure 17) at intermediate values of β disappears for

$$\bar{Z}_0 \equiv \frac{z_0}{h_{fluid}} > 0.64515, \tag{62}$$

at which point the quality factor increases monotonically with increasing β.

3.3.2. *Compressible flow*

The effects of compressibility on energy dissipation are now included. Importantly, compressibility will only affect the velocity field for the off-axis flow problem, as discussed above. However, since the total flow is given by superposition of the off-axis and on-axis problems, compressibility can affect the entire quality factor. In figure 18, results are presented for a typical normalized wavenumber of $\gamma = 0.03$, and for a range of different off-axis positions $\bar{Z}_0 \in [0, 0.1]$. Again, we consider the practical case where $L_c = L$.

Note that the quality factor in figure 18 is unaffected by off-axis channel placement for $\beta > \beta_{min} = 46.434$, and is therefore independent of fluid compressibility. This indicates that inertial effects present in the on-axis flow problem dominate any off-axis phenomena. The behaviour for $\beta < \beta_{min} = 46.434$, however, is dramatically different and is strongly influenced by fluid compressibility; cf. figures 17 and 18 for $\bar{Z}_0 = 0.1$. The incompressible solution displays a clear maximum in quality factor at $\beta \approx 1$, whereas the compressible solution shows two local maxima at $\beta \approx 10$ and $\beta \approx 0.1$, and ultimately a uniform increase as β decreases. This demonstrates that even for small off-axis channel placement, fluid compressibility can have a profound effect.

Once compressibility begins to affect energy dissipation with decreasing β, the quality factor remains approximately constant over decades in β. We also observe that the quality factor exhibits small oscillations in magnitude as β varies; this is in line with the energy dissipation results for the off-axis flow problem; cf. figures 13 and 18.

https://doi.org/10.1017/S0022112009993521 Published online by Cambridge University Press

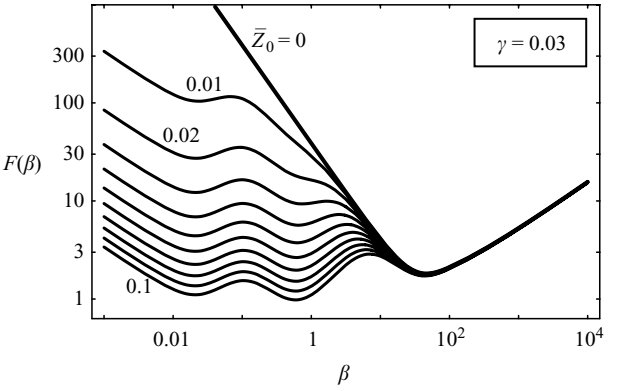


FIGURE 18. Plot of $F(\beta)$ function for quality factor for compressible flow ($\gamma = 0.03$). Exact solution (see (56a)), small β solution (see (60)) and large β solution (see (60)) are shown. Results for various off-axis placement: $\bar{Z}_0 \in [0, 0.1]$ in increments of 0.01. The top curve corresponds to $\bar{Z}_0 = 0$.

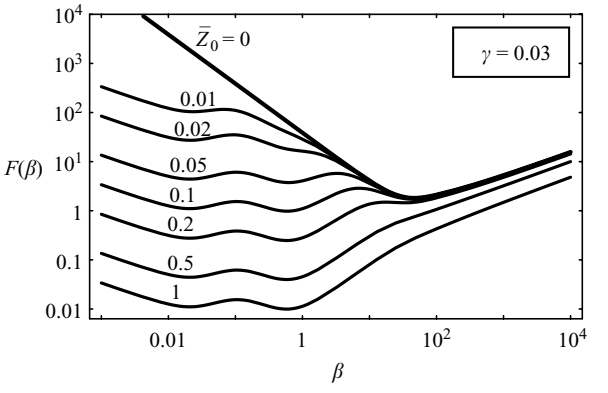


FIGURE 19. Same as figure 18 for $\bar{Z}_0 \in [0, 1]$ in increments of 0.1. The top curve corresponds to $\bar{Z}_0 = 0$.

In figure 19, we examine these effects for larger $\bar{Z}_0$ corresponding to off-axis channel placements up to one channel thickness. From these results it is clear that the quality factor always ultimately increases at lower β, regardless of the value of $\bar{Z}_0$. This behaviour contrasts directly with that for incompressible flow, for which the quality factor decreases monotonically with decreasing β for small β. We also see a slight reduction in the quality factor for $\beta > \beta_{min} = 46.434$, which is in line with the incompressible result; see (60).

As β decreases below β_{min}, we can observe two distinct local maxima in figures 18 and 19. The position of the maximum closest to $\beta_{min} = 46.434$ corresponds to the onset of the effects of off-axis channel flow, which enhances dissipation due to the pumping of fluid into and out of the channel. The second maximum furthest from β_{min} occurs at a single value of β, regardless of the off-axis channel position $\bar{Z}_0$ and coincides with the energy dissipation minimum discussed in figure 13; note that energy dissipation is inversely proportional to the quality factor. We remind the reader that this phenomenon originates from competing compressibility effects in the off-axis

https://doi.org/10.1017/S0022112009993521 Published online by Cambridge University Press

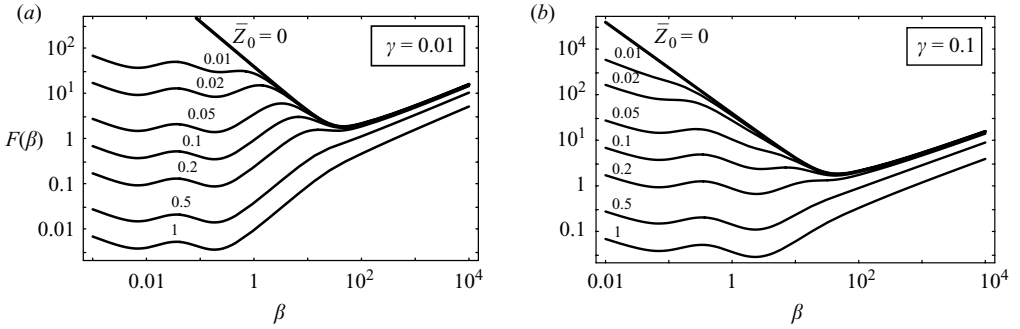


FIGURE 20. Same as figure 19 for $\gamma = 0.01, 0.1$.

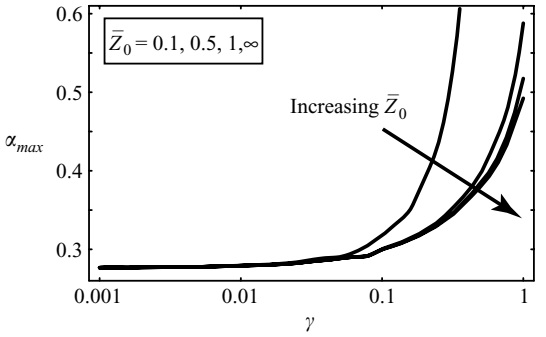


FIGURE 21. Plot showing variation in α_{max} as a function of γ for $\bar{Z}_0 = 0.1, 0.5, 1, \infty$. Value for α_{max} decreases with increasing $\bar{Z}_0$.

channel system and occurs at $\alpha = \gamma/\beta \sim 0.3$. Note that we require $\alpha \sim O(1)$ for the effects of fluid compressibility to be significant; see (32).

In figure 20, we examine the effects of varying compressibility at fixed off-axis channel position $\bar{Z}_0$. Note that compressibility significantly modifies the behaviour for $\beta < \beta_{\min} = 46.434$ and reduces dissipation due to off-axis channel placement, i.e. the quality factor *increases with increasing* γ. Furthermore, the maxima in $F(\beta)$ previously observed for incompressible flow are displaced in β space. In particular, the leftmost maximum arising from competing compressibility effects in the off-axis problem now appears at different values of β. Significantly, the value of α at which this maximum occurs is approximately constant regardless of the value of $\bar{Z}_0$ and γ for $\gamma < 0.1$, as illustrated in figure 21. In this regime, the maximum occurs at

$$\alpha_{max} = \frac{\gamma}{\beta} = \frac{\omega\mu}{\rho c^2}\left(\frac{L}{h_{fluid}}\right)^2 = 0.287, \quad \gamma \to 0. \tag{63}$$

The observed increase in α_{max} for higher values of γ is due to inertial effects in the fluid becoming increasingly important; note that β increases with increasing γ since $\beta = \gamma/\alpha$. Importantly, the physical origin of this maximum is independent of the on-axis problem, but the competing effects of the on-axis and off-axis problems can affect the position of this maximum. This explains the observed deviation in α_{res} with decreasing $\bar{Z}_0$. In the formal limit $\bar{Z}_0 \to \infty$, α_{res} plateaus to a constant value for fixed γ; see figure 21.

https://doi.org/10.1017/S0022112009993521 Published online by Cambridge University Press

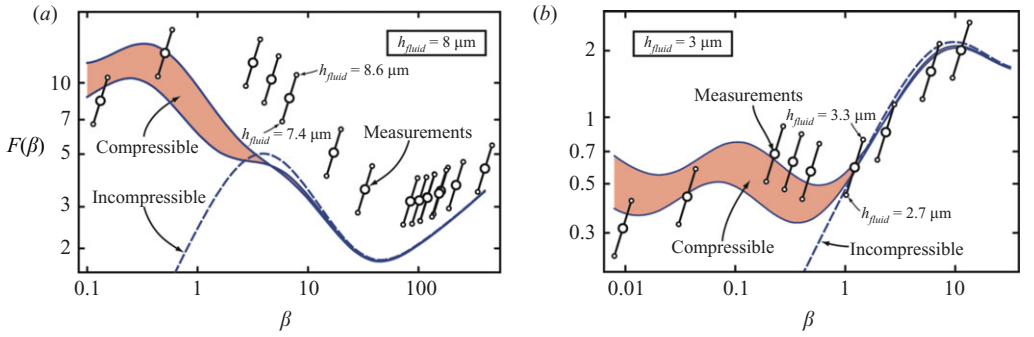


FIGURE 22. Comparison of theoretical models (lines) with measurements (circles) for cantilever A and B defined below. A glycerol/water mixture was used. Compressible model (solid line); upper trace: speed of sound $c = 1500\,\mathrm{m\,s^{-1}}$ (water), lower trace $c = 1850\,\mathrm{m\,s^{-1}}$ (glycerol). Incompressible model (dashed line). Systematic uncertainty in fluid channel thickness used to evaluate $F(\beta)$ from measurements of Q is indicated; see (55). This uncertainty allows the central large dots to be *collectively shifted* within the prescribed bounds, along the slanted lines, as shown. Q measured to $< 1\,\%$ uncertainty (Burg *et al.* 2009). (*a*) Cantilever A with 8 μm channel ($\bar{Z}_0 = 0.06$); (*b*) cantilever B with 3 μm channel ($\bar{Z}_0 = 0.14$).

3.4. *Experiments and comparison*

We now compare the predictions of the above theory with measurements taken on two different cantilevers using a glycerol/water mixture; this enables the inertia parameter β to be varied over 3 orders of magnitude. The two cantilevers have different fluid channel and cantilever thickness, but are identical otherwise. The oscillation amplitude was systematically varied to ensure that the linear limit was observed. In all cases, the measured quality factors and resonant frequencies were found to be independent of the oscillation amplitude as required; maximum oscillation amplitude used was ∼50 nm. The measured quality factors in the presence and absence of liquid are given in figure 2 of Burg *et al.* (2009), and all other experimental details are included in that reference.

Properties of the two cantilevers used are:

A. Channel: $h_{fluid} = 8 \pm 0.6\,\mu\mathrm{m}$, $b_{fluid} = 16 \pm 0.25\,\mu\mathrm{m}$, $L = 204 \pm 0.5\,\mu\mathrm{m}$, $L_c = 207.5 \pm 0.25\,\mu\mathrm{m}$; Cantilever: $h_{cant} = 12 \pm 1.5\,\mu\mathrm{m}$, $b_{cant} = 33 \pm 0.25\,\mu\mathrm{m}$, length: $210 \pm 0.5\,\mu\mathrm{m}$, resonant frequency (cantilever filled with air): $f_{res} = 426.8\,\mathrm{kHz}$.

B. Channel: $h_{fluid} = 3 \pm 0.3\,\mu\mathrm{m}$, $b_{fluid} = 16 \pm 0.25\,\mu\mathrm{m}$, $L = 204 \pm 0.5\,\mu\mathrm{m}$, $L_c = 207.5 \pm 0.25\,\mu\mathrm{m}$; Cantilever: $h_{cant} = 7 \pm 1.5\,\mu\mathrm{m}$, $b_{cant} = 33 \pm 0.25\,\mu\mathrm{m}$, length: $210 \pm 0.5\,\mu\mathrm{m}$, resonant frequency (cantilever filled with air): $f_{res} = 212.5\,\mathrm{kHz}$.

Since off-axis placement Z_0 of the fluid channel is unknown, it is used as a fitting parameter in the following comparison. Critically, the theoretical solution depends strongly on Z_0, as illustrated in figures 18–20. This enhances the precision in fitting Z_0, which can then be compared with expected values due to fabrication tolerances, as we shall discuss below.

The precision of measured values for $F(\beta)$ shown in figure 22 is primarily limited by that of the channel thickness h_{fluid} (which is known to within ∼10 %). This is because the relation between the quality factor Q and $F(\beta)$ depends on the cube of h_{fluid}; see (55). Systematic uncertainty in h_{fluid} will therefore collectively shift the measured values of $F(\beta)$, as illustrated in figure 22; small open circles indicate the bounds of this shift, whereas the large circles indicate the expected values. The statistical error in measurements of Q is less than 1 % (see Burg *et al.* 2009) and is indiscernible in

https://doi.org/10.1017/S0022112009993521 Published online by Cambridge University Press

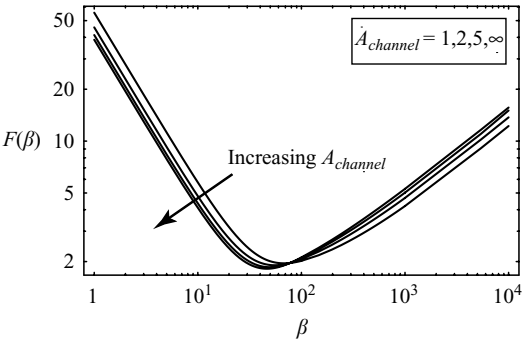


FIGURE 23. Plot of $F(\beta)$ function for quality factor as a function of the channel aspect ratio $A_{channel}$ using the exact solution (A 2).

figure 22. As such, the observed variations in the measured $F(\beta)$ as a function of β, for a fixed h_{fluid}, completely dominate the measurement error.

In figure 22(*a*), we present a comparison of the theoretical model with measurements for cantilever A, which possesses a fluid channel of square cross-section. We remind the reader that the model is derived using an Euler–Bernoulli/lubrication formulation, and as such, is formally valid for cases where the cantilever length L greatly exceeds the cantilever width b_{cant}, and where the channel width b_{fluid} greatly exceeds its thickness h_{fluid}. Cantilever A possesses the properties $L/b_{cant} \approx 6$ and $b_{fluid}/h_{fluid} \approx 2$, which is somewhat outside the expected regime of validity of the model. Nonetheless, we observe from figure 22(*a*) that the (compressible) model predicts the salient features of the response, when a (scaled) off-axis channel position of $\bar{Z}_0 = 0.06$ is chosen. This corresponds to $Z_0 = 0.5\,\mu\text{m}$, which is in line with the expected uncertainty in the microfabrication process; note that Z_0 cannot be measured directly in these devices. For completeness, variations in the fluid compressibility between the expected bounds for glycerol/water are also shown in figure 22 (shaded regions). This results in a relatively minor variation in comparison to the incompressible theory, which is unable to describe the measurements in the low β regime, regardless of the choice of $\bar{Z}_0$.

Interestingly, we find that at high β, the measured quality factor exceeds the model prediction, indicating that dissipation in the real system is less than that predicted. Use of the arbitrary channel aspect ratio theory (see the Appendix) in this regime does not reconcile theory and measurements; cf. figures 22(*a*) and 23. Importantly, the arbitrary channel aspect ratio theory in the Appendix still requires that the cantilever length greatly exceed its width, and as such, the comparison between theory and measurements indicates that finite L/b_{cant} and L/h_{cant} effects may be behind the observed discrepancy between theory and measurements.

A possible explanation for this observed reduction in dissipation (higher Q) in comparison to the theoretical model is now outlined. A cantilever of finite length is expected to provide extra constraints on the on-axis flow, particularly at the free end of the cantilever where the flow must move in tandem with the beam. This will reduce the strain rate in that region (of maximum amplitude) and decrease the overall energy dissipation; this is observed in both the low and high β incompressible on-axis regimes ($3 < \beta < 300$). For lower β, the off-axis (pumping) flow dominates and the model yields results in reasonable agreement with measurements. We emphasize, however, that the precise mechanism giving rise to the measured discrepancy can only

https://doi.org/10.1017/S0022112009993521 Published online by Cambridge University Press

be rigorously established by calculating the next order correction for finite L/b_{cant} and L/h_{cant}; see § 3.5.

Complementary results for cantilever B are given in figure 22(*b*). In comparison to cantilever A, this cantilever possesses a significantly thinner fluid channel with $b_{fluid}/h_{fluid} \approx 5$. We note that the agreement between theory and measurements is greatly improved, with the model accurately predicting the features of the measured response. In this case, an off-axis channel position of $\bar{Z}_0 = 0.14$ ($Z_0 = 0.4\,\mu\text{m}$) is required to yield good agreement between measurements and theory; this absolute offset is similar to that for cantilever A and is again in line with expected uncertainty in channel placement. This improvement in agreement is consistent with the assumption inherent in the model that the fluid channel width greatly exceeds its thickness. Again, we find that the incompressible theory is incapable of predicting the measurements with the leftmost maximum in figure 22(*b*) absent (see dashed line). Fluid compressibility is therefore found to be of paramount importance in describing the dynamics of these devices, and the above comparisons serve to demonstrate the validity of the new model.

It is important to note that the quality factor due to dissipation in the fluid can be comparable in magnitude to the intrinsic quality factor of the cantilever structure, as observed by Burg *et al.* (2007). This feature can result in identical quality factors when air or water is used, as we now discuss. Injecting water into the fluid channel increases the mass of the cantilever, which lowers the resonant frequency. This increases the intrinsic quality factor (since it is a scaled quantity) provided the intrinsic damping coefficient is frequency independent, which is assumed in the above experimental comparison. As a result, the intrinsic quality factor of the device with water in the channel is higher than that with air, i.e. $Q^{intrinsic}_{WATER} > Q^{intrinsic}_{AIR}$. Importantly, the fluid quality factor for air is orders of magnitude higher than the intrinsic quality factor $Q^{intrinsic}_{AIR}$, whereas for water the intrinsic and fluid quality factors are of comparable magnitude. The net effect is that the total quality factor in air is well described by the intrinsic value $Q^{intrinsic}_{AIR}$, whereas in water the total quality factor is lower than $Q^{intrinsic}_{WATER}$. These competing effects can conspire to give identical quality factors in air and water, as observed by Burg *et al.* (2007).

3.5. *Further theoretical considerations*

We close by discussing some technical issues that are pertinent to (i) further theoretical development and (ii) implementation of the theoretical model in practice. Importantly, the model presented in § 2 has been derived self-consistently in the formal asymptotic limit of narrow channel thickness and infinite cantilever length, i.e. $L/b_{cant} \gg 1$, $L/h_{cant} \gg 1$ and $b_{fluid}/h_{fluid} \gg 1$, and theories of equal order in both fluid and solid mechanics have been used throughout. As such, all higher-order effects that depend on finite channel thickness or cantilever length have been implicitly ignored. These effects may become significant for cantilevers whose length does not greatly exceed their width and thickness, or when the fluid viscosity is very large (very small β), as we discuss below. Significantly, higher-order corrections due to these competing effects are of equal order and, therefore, must be implemented simultaneously for development of a self-consistent theory. We now outline the various competing higher-order effects.

First, reducing the length of the cantilever, at constant thickness, will enhance the effects of shear deformation that are implicitly ignored in Euler–Bernoulli beam theory. These constitute a correction of $O(h_{cant}/L)$ which can be tackled approximately using higher-order theories such as Timoshenko beam theory (Timoshenko & Young

https://doi.org/10.1017/S0022112009993521 Published online by Cambridge University Press

1968). Second, finite channel length ratio h_{fluid}/L requires consideration of end-effects (also of $O(h_{cant}/L)$), which are completely ignored in the present theory. This would require consideration of both inlet channel effects and relaxation of the lubrication assumption used throughout. Third, curvature effects in the beam, which have also been ignored, constitute a correction of $O(h_{cant}/L)$. Consequently, these three phenomena contribute terms of equal order to the final solution and must be considered simultaneously.

From (5) and (19), a scaling analysis of curvature effects reveals that they become important when the viscous penetration depth becomes comparable to $\sqrt{h_{fluid}L}$, i.e. $\beta \leqslant O(h_{fluid}/L)$. This inequality is only satisfied in current devices (Burg *et al.* 2007) when the fluid viscosity greatly exceeds that of water, i.e. when β is less than ~ 0.1; this corresponds to a viscosity greater than $\sim 100\times$ that of water. While clearly not providing a limitation in current devices in practical (biological) applications (Burg *et al.* 2007), miniaturization by 2 orders of magnitude to nanoscale dimensions would provide a regime where such higher-order effects become important. The above-mentioned extensions would therefore constitute an important future direction in theoretical development.

4. Conclusions

We have theoretically investigated the fluid dynamics in microfluidic cantilever beam resonators (Burg *et al.* 2007). This involved development of a self-consistent theoretical model that rigorously accounts for both the elastic deformation of the beam and the resulting flow field in the channel. The principal underlying assumptions in the model are that (i) the cantilever length greatly exceeds its width, so that Euler–Bernoulli beam theory and a commensurate lubrication model for the fluid flow are applicable, and (ii) the channel width greatly exceeds its thickness. Consequently, the model presents a leading-order theory for this new class of microcantilever/fluid system.

It was found that the flow dynamics of these devices depend not only on the fluid density and viscosity but also on the fluid compressibility. This latter feature is not exhibited in conventional microcantilevers immersed in fluids. As a result of strongly competing effects in the flow, energy dissipation was found to be a non-monotonic function of the fluid viscosity. This enables miniaturization of the device while reducing energy dissipation. This highly desirable attribute contrasts strongly with conventional devices, whose quality factor is degraded upon miniaturization, and these new devices thus present a most favourable structure.

The non-monotonicity in energy dissipation results from competing effects due to fluid inertia and fluid compressibility. In the high inertia regime, enhanced dissipation is predicted with increasing viscosity, as may be expected intuitively. In the low inertia regime, however, a combination of off-axis and on-axis flow phenomena contributes to oscillations in energy dissipation with increasing viscosity. This behaviour depends implicitly on the channel dimensions and its placement within the cantilever. These generic features in turn enable considerable tuning of the energy dissipation landscape through minor adjustments in the device structure.

The validity of the new theoretical model was demonstrated by comparison with detailed measurements using fluids whose viscosities were varied over 3 orders of magnitude. The characteristic features of the quality factor were well described by the new model, which in turn explains the dominant underlying physical mechanisms. Finally, a discussion was presented of the limitations and possible future extensions of

https://doi.org/10.1017/S0022112009993521 Published online by Cambridge University Press

the model. These involve development of a self-consistent theory to next order in the channel length ratio. The theoretical model presented here is expected to be of significant practical value in the design, application and development of these new devices.

This work was supported by the Institute for Collaborative Biotechnologies from the US Army Research Office, the NIH Cell Decision Process Center, and by the Australian Research Council Grants Scheme.

Appendix

In this Appendix, we examine the on-axis problem and relax the restriction that the channel width greatly exceeds its thickness. In so doing, we present the exact solution to the on-axis problem for a channel of arbitrary aspect ratio (channel width/channel thickness). This is easily obtained by adding an extra velocity component to (13) that accounts for the no-slip condition at the sidewalls of the channel, thus eliminating the slip velocity at $y = \pm b_{fluid}/2$. This is performed using an eigenfunction expansion to yield

$$\boldsymbol{v} = A\left(\bar{z} - \frac{\sinh\left((1-\mathrm{i})\sqrt{\frac{\beta}{2}}\bar{z}\right)}{\sinh\left(\frac{1-\mathrm{i}}{2}\sqrt{\frac{\beta}{2}}\right)} + \sum_{n=1}^{\infty} \frac{2\mathrm{i}\beta(-1)^{n+1}\cosh\left(\sqrt{(2n\pi)^2 - \mathrm{i}\beta}\,\bar{y}\right)\sin(2n\pi\bar{z})}{n\pi((2n\pi)^2 - \mathrm{i}\beta)\cosh\left(\frac{A_{channel}}{2}\sqrt{(2n\pi)^2 - \mathrm{i}\beta}\right)}\right) \times \hat{\boldsymbol{x}} + (U_0 + A(\bar{x} - \bar{x}_0))\hat{\boldsymbol{z}}, \quad (A\,1)$$

where the pressure remains identical to the inviscid solution given in (9), the y-coordinate is again scaled by the thickness of the channel h_{fluid} and the aspect ratio of the channel (width/thickness) is $A_{channel}$. Importantly, (A 1) is applicable to cantilevers with multiple channels provided b_{fluid} is taken as the sum of all channel widths, while retaining $A_{channel}$ as the true aspect ratio of each channel; each channel is assumed identical.

The exact solution for the function $F(\beta)$ defined in (16) for the quality factor can be written as

$$F(\beta) = 0.10758 A_{channel}\beta\left|\frac{A}{h_{fluid}}\right|^2\left(\int_{-A_{channel}/2}^{A_{channel}/2}\int_{-1/2}^{1/2} \boldsymbol{e} : \boldsymbol{e}^*\,\mathrm{d}\bar{z}\,\mathrm{d}\bar{y}\right)^{-1}. \quad (A\,2)$$

The asymptotic forms for $F(\beta)$ in the limits of small and large inertia can be evaluated directly from (A 2) to give

$$F(\beta) = \begin{cases} \dfrac{38.73}{\beta}\left(1 - \dfrac{90}{A_{channel}}\displaystyle\sum_{n=1}^{\infty}\frac{\tanh(n\pi A_{channel})}{(n\pi)^5}\right)^{-1} & : \beta \ll 1, \\ 0.1521\sqrt{\beta}\left(1 + \dfrac{1}{3A_{channel}}\right)^{-1} & : \beta \gg 1. \end{cases} \quad (A\,3)$$

For the practical case of $A_{channel} \geqslant 1$, (A 3) is well approximated by

$$F(\beta) = \begin{cases} \dfrac{38.73}{\beta}\left(1 - \dfrac{0.3050}{A_{channel}}\right)^{-1} & : \beta \ll 1, \\ 0.1521\sqrt{\beta}\left(1 + \dfrac{1}{3A_{channel}}\right)^{-1} & : \beta \gg 1. \end{cases} \quad (A\,4)$$

https://doi.org/10.1017/S0022112009993521 Published online by Cambridge University Press

From (A 4), we observe that for a square channel ($A_{channel} = 1$), the solution differs from the limiting case of $A_{channel} \gg 1$ by only $\sim 30\,\%$ in the limits of small and large inertia. Interestingly, we find that by reducing $A_{channel}$, the quality factor increases for small inertia, whereas for large inertia the quality factor decreases. The effect at low inertia is due to the sidewalls limiting the inertial mechanism (secondary flow) that drives dissipation, whereas at high inertia all dissipative effects are contained in thin viscous boundary layers at the surfaces and are thus additive. These properties are manifested in the entire $F(\beta)$ curve shifting to higher values of β as the channel aspect ratio $A_{channel}$ is reduced; see figure 23. Nonetheless, this shift is small and has negligible effect on the minimum value of $F(\beta)$. The critical value of β where this minimum occurs is $\beta = 46.4$ for $A_{channel} \gg 1$ and increases monotonically to $\beta = 67.6$ at $A_{channel} = 1$.

We therefore conclude that finite channel aspect ratio $A_{channel}$ exerts a relatively small effect on the overall dynamics of the on-axis problem.

REFERENCES

Basak, S., Raman, A. & Garimella, S. V. 2006 Hydrodynamic loading of microcantilevers vibrating in viscous fluids. *J. Appl. Phys.* **99**, 114906.

Batchelor, G. K. 1974 *An Introduction to Fluid Dynamics*. Cambridge University Press.

Berger, R., Gerber, C., Lang, H. P. & Gimzewski, J. K. 1997 Micromechanics: a toolbox for femtoscale science: 'Towards a laboratory on a tip'. *Microelectron. Engng* **35**, 373–379.

Binnig, C., Quate, C. F. & Gerber, C. 1986 Atomic force microscope. *Phys. Rev. Lett.* **56**, 930–933.

Burg, T. P., Godin, M., Knudsen, S. M., Shen, W., Carlson, G., Foster, J. S., Babcock, K. & Manalis, S. R. 2007 Weighing of biomolecules, single cells and single nanoparticles in fluid. *Nature* **446**, 1066–1069.

Burg, T. P. & Manalis, S. R. 2003 Suspended microchannel resonators for biomolecular detection. *Appl. Phys. Lett.* **83**, 2698–2700.

Burg, T. P., Sader, J. E. & Manalis, S. R. 2009 Non-monotonic energy dissipation in microfluidic resonators. *Phys. Rev. Lett.* **102**, 228103.

Butt, H.-J., Siedle, P., Seifert, K., Fendler, K., Seeger, T., Bamberg, E., Weisenhorn, A., Goldie, K. & Engel, A. 1993 Scan speed limit in atomic force microscopy. *J. Microsc.* **169**, 75–84.

Chon, J. W. M., Mulvaney, P. & Sader, J. E. 2000 Experimental validation of theoretical models for the frequency response of atomic force microscope cantilever beams immersed in fluids. *J. Appl. Phys.* **87**, 3978–3988.

Chu, W.-H. 1963 Vibration of fully submerged cantilever plates in water. *Tech. Rep.* No. 2, DTMB, Contract NObs-86396(X), Southwest Research Institute, San Antonio, Texas.

Clarke, R. J., Cox, S. M., Williams, P. M. & Jensen, O. E. 2005 The drag on a microcantilever oscillating near a wall. *J. Fluid Mech.* **545**, 397–426.

Crighton, D. G. 1983 Resonant oscillations in fluid-loaded struts. *J. Sound Vib.* **87**, 429–437.

Enoksson, P., Stemme, G. & Stemme, E. 1996 Silicon tube structures for a fluid-density sensor. *Sens. Actuators* A **54**, 558–562.

Fu, Y. & Price, W. G. 1987 Interactions between a partially or totally immersed vibrating cantilever plate and the surrounding fluid. *J. Sound Vib.* **118**, 495–513.

Fukuma, T., Kobayashi, K., Matsushige, K. & Yamada, H. 2005 True atomic resolution in liquid by frequency-modulation atomic force microscopy. *Appl. Phys. Lett.* **87**, 034101.

Green, C. P. & Sader, J. E. 2005 Small amplitude oscillations of a thin beam immersed in a viscous fluid near a solid surface. *Phys. Fluids* **17**, 073102.

Landweber, L. 1967 Vibration of a flexible cylinder in a fluid. *J. Ship Res.* **11**, 143–150.

Lavrik, N. V., Sepaniak, M. J. & Datskos, P. G. 2004 Cantilever transducers as a platform for chemical and biological sensors. *Rev. Sci. Instrum.* **75**, 2229–2253.

Lindholm, U. S., Kana, D. D., Chu, W.-H. & Abramson, H. N. 1965 Elastic vibration characteristics of cantilever plates in water. *J. Ship Res.* **9**, 11–22.

https://doi.org/10.1017/S0022112009993521 Published online by Cambridge University Press

Naik, T., Longmire, E. K. & Mantell, S. C. 2003 Dynamic response of a cantilever in liquid near a solid wall. *Sens. Actuators* A **102**, 240–254.

Paul, M. R. & Cross, M. C. 2004 Stochastic dynamics of nanoscale mechanical oscillators immersed in a viscous fluid. *Phys. Rev. Lett*. **92**, 235501.

Sader, J. E. 1998 Frequency response of cantilever beams immersed in viscous fluids with applications to the atomic force microscope. *J. Appl. Phys.* **84**, 64–76.

Sparks, D., Smith, R., Straayer, M., Cripe, J., Schneider, R., Chimbayo, A., Anasari, S. & Najafi, N. 2003 Measurement of density and chemical concentration using microfluidic chip. *Lab Chip*. **3**, 19–21.

Timoshenko, S. & Young, D. H. 1968 *Elements of Strength of Materials*. D. Van Nostrand.

Westberg, D., Paul, O., Anderson, G. & Baltes, H. 1997 A CMOS-compatible fluid density sensor. *J. Micromech. Microengng* **7**, 253–255.

Yasumura, K. Y., Stowe, T. D., Chow, E. M., Pfafman, T., Kenny, T. W., Stipe, B. C. & Rugar, D. 2000 Quality factors in micron- and submicron-thick cantilevers *J. Microelectromech. Syst*. **9**, 117–125.

https://doi.org/10.1017/S0022112009993521 Published online by Cambridge University Press